



Platelet-derived extracellular vesicles ameliorate intervertebral disc degeneration by alleviating mitochondrial dysfunction

Zhanqiu Dai^{a,b,c,d,1}, Chen Xia^{b,c,d,1}, Tingxiao Zhao^{d,1}, Haoli Wang^{b,c}, Hongsen Tian^{b,c}, Ouyuan Xu^e, Xunbin Zhu^{a,***}, Jun Zhang^{d,**}, Pengfei Chen^{b,c,f,*}

^a Department of Orthopaedics, The Second Affiliated Hospital of Bengbu Medical College, Anhui, China

^b Department of Orthopaedic Surgery, Sir Run Run Shaw Hospital, Zhejiang University School of Medicine, Hangzhou, China

^c Key Laboratory of Musculoskeletal System Degeneration and Regeneration Translational Research of Zhejiang Province, China

^d Department of Spine Surgery, Zhejiang Provincial People's Hospital, Hangzhou Medical College People's Hospital, Hangzhou, Zhejiang, China

^e College of Animal Sciences, Zhejiang University, Hangzhou, Zhejiang, China

^f Hangzhou OrigO Biotechnology Co. Ltd., Hangzhou, Zhejiang, China

ARTICLE INFO

Keywords:

Intervertebral disc degeneration
Nucleus pulposus
Platelets
Vesicles
Reactive oxygen species
Mitochondrial dysfunction

ABSTRACT

Mitochondrial dysfunction causes the production of reactive oxygen species (ROS) and oxidative damage, and oxidative stress and inflammation are considered key factors causing intervertebral disc degeneration (IVDD). Thus, restoring the mitochondrial dysfunction is an attractive strategy for treating IVDD. Platelet-derived extracellular vesicles (PEVs) are nanoparticles that target inflammation. Moreover, the vesicles produced by platelets (PLTs) have considerable anti-inflammatory effects. We investigate the use of PEVs as a therapeutic strategy for IVDD in this study. We extract PEVs and evaluate their properties; test their effects on H₂O₂-induced oxidative damage of nucleus pulposus (NP) cells; verify the role of PEVs in repairing H₂O₂-induced cellular mitochondrial dysfunction; and demonstrate the therapeutic effects of PEVs in a rat IVDD model. The results confirm that PEVs can restore impaired mitochondrial function, reduce oxidative stress, and restore cell metabolism by regulating the sirtuin 1 (SIRT1)-peroxisome proliferator-activated receptor gamma coactivator 1α (PGC1α)-mitochondrial transcription factor A (TFAM) pathway; in rat models, PEVs retard the progression of IVDD. Our results demonstrate that the injection of PEVs can be a promising strategy for treating patients with IVDD.

1. Introduction

Lower back pain (LBP) is one of the most common musculoskeletal disorders in modern society [1]. Earlier epidemiological studies have confirmed that the prevalence of LBP increases with age, which can lead to significant family and social burden [1,2]. Intervertebral disc degeneration (IVDD) has been identified as a major cause of LBP. Disc degeneration is characterized by disc collapse, fracture of the fibrous annulus (AF), disc dehydration, which includes loss of proteoglycans and water in the nucleus pulposus (NP), calcification of the cartilage end plate, and changes in the extracellular matrix (ECM) [3–6]. The current conservative treatment and surgical interventions for IVDD cannot halt or reverse the progression of disc degeneration, and they are more likely to

exacerbate adjacent disc injury [7–10]. Treatment strategies to prevent or delay the progression of degeneration at an early stage while protecting the physiological stability of the intervertebral disc (IVD) remain under investigation [11]. Although there is a wide range of pharmaceutical drugs available for treating IVDD, there are certain drawbacks, which include the absence of an abundant blood supply to the IVD [12], prolonged failure caused by extracellular expansion of the drug, failure to target delivery in a timely manner, and side effects such as the inflammation of the adjacent tissue after the local administration of the treatment [13]. In the field of basic research, several reports have been published on cellular exosome therapy for IVDD; this therapy has relatively good biocompatibility and low immunogenicity [14–16]. However, the active protein component in exosome therapy cannot be clarified,

* Corresponding author. Sir Run Run Shaw Hospital, Qingchun East Road 3#, Hangzhou, 310000; China.

** Corresponding author. Department of Spine Surgery, Zhejiang Provincial People's Hospital, Shangtang Road 158#, Hangzhou, Zhejiang, 310014, China.

*** Corresponding author. The Second Affiliated Hospital of Bengbu Medical College, Longhua Road 633#, Anhui, 233030, China.

E-mail addresses: zhuxb22@163.com (X. Zhu), spinezhangjun@aliyun.com (J. Zhang), pengfei_chen@zju.edu.cn (P. Chen).

¹ These authors have contributed equally.

and it remains a great challenge to accurately, effectively, and selectively identify and isolate the exosomes [17].

Platelet-rich plasma (PRP) is an autologous cell-derived therapy [18]. At present, PRP and pure PRP without leukocytes are being used in the clinical treatment of various diseases [19,20]. Despite the large variety of applications, the efficacy of regenerative treatments using PRP remains controversial owing to the absence of large controlled clinical trials [21]. PRP comprises a complex list of components, including pro-inflammatory factors, anti-inflammatory factors, chemokines, and transforming growth factors. During the study on the specific molecular efficacy of PRP, the exact effective proteins of PRP involved in clinical treatment are unclear [22]. Moreover, the underlying mechanisms, principles, and safety of PRP therapy for clinical use remain to be elucidated [18]. An autologous product that does not specify its formulation and composition [23,24] has variations in its composition in terms of platelets (PLTs), white blood cells (WBC), and red blood cells (RBC) [25,26]. Consequently, the consensus on PRP bio-formulations is nonexistent at present. Sufficiently powered and well-documented clinical research is needed to determine the full potential and therapeutic molecular efficacy of PRP in a variety of indications [18].

Platelets (PLTs) are anucleate blood cells produced by the cytoplasmic lysis of mature megakaryocytes in the bone marrow [27]. These cells are increasingly recognized as pivotal participants in numerous pathophysiological processes, including thrombosis, inflammation, atherogenesis, and tumor growth, and metastasis [28,29]. In addition, related research has reported that PLTs can enhance the wound-healing activity of mesenchymal stem cells (MSCs) and provide them with energy for metabolism by functional mitochondria [30,31]. These studies have demonstrated that PLTs can be used as an adjuvant for improving therapeutic efficacy. However, PLTs are easily affected by various conditions (such as temperature, shake, and pollution) during storage and transportation, resulting in an inflammatory response [32]. In these states, PLTs can be positively primed to reach an activated condition [33]. Thrombin-activated PLTs release α -granules and dense granules located in the PLT cytoplasm. The α -granules contain pro-inflammatory cytokines, such as IL-1 β , IL-6, and TNF- α , which can aggravate the local inflammatory response [34–36] and further affect the therapeutic effect of PLTs [37–39]. Thus, further studies are required to prevent the pro-inflammatory effects of PLTs and better utilize their therapeutic efficacy.

Nanomaterial therapy is a current trend in nanomedicine [40]. PLT-derived extracellular vesicles (PEVs), also known as PLT dust and PLT-derived particles, are a heterogeneous group of small, lipid-bound nanoparticles that play a key role in mediating pathological and physiological processes [41–45]. In recent years, PEVs have been identified as unique therapeutic modalities that demonstrate advantages in hemostasis, inflammation, and tissue repair, as well as drug delivery carriers [45]. A study has reported that PEVs secreted lower levels of inflammatory cytokines (IL-1 β , IL-6, and TNF- α) compared to activated PLTs. The low level of cytokine releases from PEVs may be due to the fact that α -granules do not exist in PEVs [39,46]. Notably, PEVs can penetrate tissue barriers, such as the synovium, lymph, and bone marrow, to achieve specific therapeutic effects [37]. Moreover, the majority of PEVs are stable structures with diameters in the range of 100–200 nm; such structures retain some effective mitochondrial proteins and are more easily ingested by cells [47–49]. Thus, PEVs exhibit non-negligible therapeutic potential for injury, inflammation, and tissue repair [50–52]. However, mesenchymal stem cell (MSC)-derived EVs are currently the main research direction in nanomedicine [53,54], and limited attention has been focused on the study of PEVs in the treatment of degenerative diseases. We believe that this nanomaterial therapy may provide more potential therapeutic prospects in the future.

Oxidative stress in NP cells is a cause of irreversible IVDD [55]. Mitochondria are the target organelles of intracellular reactive oxygen species (ROS), and mitochondrial dysfunction leads to intracellular metabolic imbalance [55,56]. As the powerhouse of the cell [57],

mitochondria can provide energy for a range of activities in the form of adenosine triphosphate (ATP) molecules [58,59]. The impairment of mitochondrial function is strongly associated with degenerative diseases [60–62]. Inflammatory degeneration is exacerbated because of an insufficient ATP supply when mitochondria are impaired [63,64]. Fen et al. demonstrated that the mitochondrial structure and function were damaged in the pathological process of IVDD [65,66]. Inflammation or mechanical injury alters the mitochondrial membrane potential, which further reduces cell proliferation and induces apoptosis; this ultimately leads to IVDD [67]. Therefore, repairing damaged mitochondria by inhibiting oxidative stress is considered a valid option for delaying IVDD.

AMP-activated protein kinase (AMPK) is a highly conserved sensor that detects elevated levels of AMP and ADP caused by mitochondrial ATP depletion [68]. It is an important molecular target for the treatment of degenerative diseases. During inflammation, AMPK activation protects mitochondrial function by promoting the expression of sirtuin 1 (SIRT1) [69,70]. In addition, peroxisome proliferator-activated receptor gamma coactivator 1 α (PGC1 α) is a regulatory mechanism required for AMPK in NP cells [71]. Increased PGC1 α expression reverses mitochondrial biogenesis, oxidative phosphorylation, and intracellular ATP levels in degenerative cells [72]. Mitochondrial transcription factor A (TFAM) is a gene regulator that mitigates ROS production by wrapping around mitochondrial DNA complexes [73]; nuclear respiratory factors 1 and 2 (Nrf1 and Nrf2, respectively) are also essential for the mitochondrial biological function [25,54].

In this study, we isolated and characterized platelet-derived vesicles and investigated the role of PEVs in H₂O₂-induced oxidative stress and mitochondrial dysfunction in NP cells. Further, we used a rat IVDD model to verify the therapeutic effect of PEVs on IVDD (Fig. 1). We hypothesize that PEVs can restore mitochondrial function in NP cells through the SIRT1–PGC1 α –TFAM pathway and prevent the progression of degenerative changes in IVDD.

2. Materials and methods

2.1. Materials

Dulbecco's modified Eagle's medium (DMEM) and fetal bovine serum (FBS) were purchased from Gibco BRL (Gaithersburg, MD, USA). Aggrecan (ab3778) and Adamts5 (ab41037) were purchased from Abcam (Cambridge, USA). TSG101 (28283-1-AP), CD9 (20597-1-AP), CD63 (25682-1-AP), CD41 (24552-1-AP), Col2 α (28459-1-AP), SOX9 (67439-1-Ig), MMP3 (18165-1-AP), MMP13 (17873-1-AP), SIRT1 (13161-1-AP), PGC1 α (66369-1-Ig), TFAM (22586-1-AP), Nrf1 (12482-1-AP), Nrf2 (16396-1-AP), β actin (20536-1-AP), and GAPDH (10494-1-AP) were purchased from Proteintech® (Beijing, China).

2.2. Preparation and characterization of isolated PLTs and PEVs

PRP was prepared using a previously described method with minor modifications [74,75]. All blood specimens used in the present study were approved by the Ethical Committee of the Sir Run Run Shaw Hospital, School of Medicine, Zhejiang University. Informed consent was obtained. In brief, whole blood samples were collected from healthy donors and mixed with acid citrate dextrose solution A (ACD-A) anticoagulant (1 mL ACD-A/9 mL blood). After centrifugation at 100 \times g for 15 min, the PLT-containing plasma was collected and centrifuged at 800 \times g for 20 min. The supernatant plasma was discarded, and the PLT pellet was resuspended in residual plasma to obtain PRP (SI Fig. 1). To prepare PEVs, PLTs were mixed in phosphate buffered saline (PBS) containing ethylenediamine tetraacetic acid (EDTA, 5 mM, Sigma Aldrich) and prostaglandin e1 (PGE1, 1 mM, MCE). Next, PLTs were passed through 1000 nm and 500 nm filters, and then thrice through a 200 nm filter to obtain PEVs. Finally, the supernatant was collected for ultracentrifugation, and PEVs were enriched at 100,000 rpm for 2 h. We observed the morphology and size of PLTs and PEVs using cryo-transmission electron

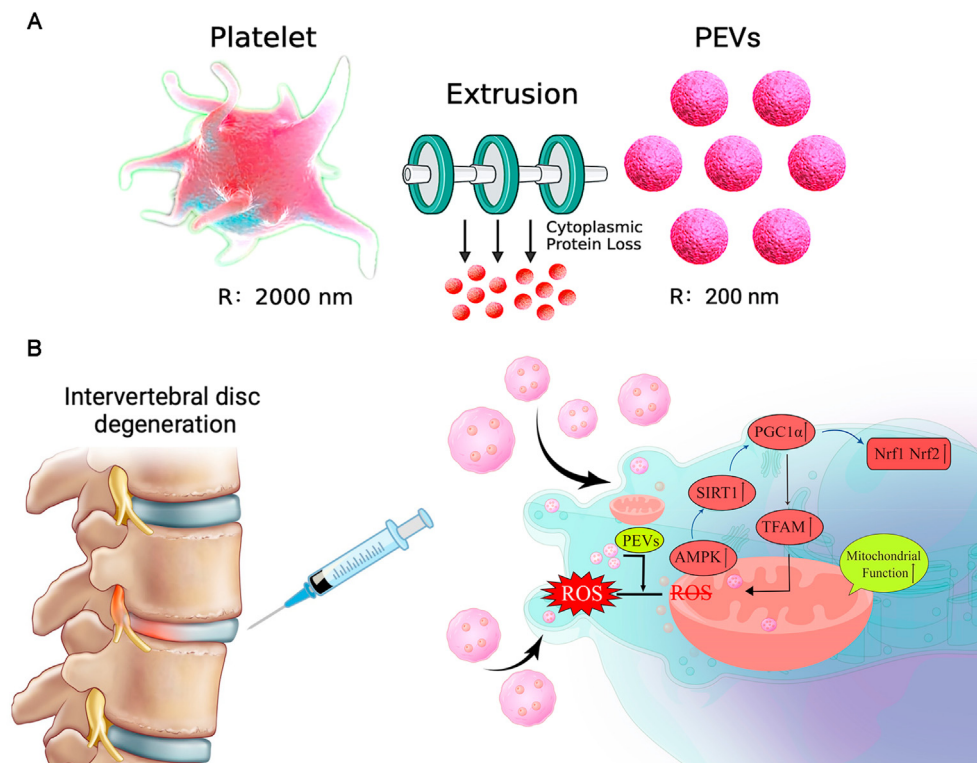


Fig. 1. (A) Illustration and technical theory of preparation of PEVs *in vitro*. (B) A schematic diagram of the IVDD retarding pathway by the local injection of PEVs reduce oxidative stress and activate the mitochondrial functional protein pathway.

microscopy (cryo-TEM, 200 kV, FEI Tecnai G2 F20, USA), and we quantified their particle size and zeta potential using dynamic light scattering (DLS). We tested the stability of the PLTs and PEVs by measuring the particle size changes at 0, 1, 3, 5, and 7 days using DLS. In addition, we extracted PLTs and PEVs proteins using a protein isolation kit (Invitrogen, Carlsbad, USA), and we quantified the protein concentration using a BCA kit (Beyotime, China). The protein expression levels of PLTs and PEVs were detected using SDS-PAGE and western blotting, respectively. Coomassie brilliant blue staining (Beyotime, China) was used to detect differences in protein expression between the PLTs and PEVs.

2.3. Evaluation of materials for cytotoxicity and proliferation

The toxicity and proliferation of NP cells incubated with PEVs were tested for 1, 3, 5, and 7 days using a CCK-8 detection kit (MCE, USA). The toxicity of the different concentrations of each inhibitor (chlorpromazine, filipin III, wortmannin, and cytochalasin D) in NP cells by CCK-8 kit assay. We added a 10 μ L CCK-8 solution to the serum-free medium of the cells, and then incubated them at 37 $^{\circ}$ C for 2 h. The absorbance at 450 nm was measured using a Varioskan LUX microplate reader (Thermo Fisher Scientific, USA). All experiments were performed in triplicate.

2.4. Cytokine detection

Production was provided by the manufacturer; 100 μ g/mL PLTs and 100 μ g/mL PEVs were activated with or without thrombin, respectively. The levels of IL-1 β and IL-6 were detected using ELISA assay kits (BMS224-2, BMS213-2, Thermo Fisher Scientific). All experiments were performed in triplicate.

2.5. Cell culture and handling

The NP cells were obtained from Sprague–Dawley rats purchased

from Cyagen Biosciences, Inc. (Shanghai, China). First, the NP tissue was macroscopically isolated from the caudal disc of 4 weeks male SD rats. Then, the tissue was digested with collagenase II for 4 h at 37 $^{\circ}$ C. The cell mixture filtered through the cell sieve was centrifuged at 1000 rpm for 5 min to obtain primary NP cells. The NP cells were cultured in DMEM supplemented with 10% FBS in a humidified incubator with 5% CO₂. The second passage of the cells was used for subsequent experiments. All cells were seeded in six-well plates and 10 cm plate. Then, the cells were divided into four groups: control group (normal control group), 200 μ M H₂O₂ treatment for 12 h (H₂O₂ group), H₂O₂ + 100 μ g/mL platelets (PLTs group), and H₂O₂ + 100 μ g/mL PEVs (PEVs group).

2.6. ROS detection and evaluation

The ROS levels in the NP cells were detected using an ROS detection kit (Beyotime, China). The NP cells were pre-treated with 200 μ M H₂O₂ for 6 h, and then each group was added with 100 μ g/mL of PLTs or PEVs for 24 h. Then, the NP cells were incubated with 20 mM 2',7'-dichlorodihydrofluorescein diacetate (DCFH-DA, Beyotime, China) for 37 $^{\circ}$ C, 20 min. Before flow cytometry analysis, the cells were washed three times with a serum-free medium. Fluorescence signal intensity was determined by the oxidative conversion of DCFH-DA. Finally, changes in intracellular ROS levels were detected by fluorescence microscopy and flow cytometry. We analyzed the results using FlowJo software. All experiments were performed with four replicates each.

2.7. Flow cytometry and TUNEL staining for cell apoptosis

The apoptosis rate of NP cells was detected using a fluorescein isothiocyanate–annexin V and propidium iodide (FITC/PI) Apoptosis Detection Kit (Yeasen, China) according to the manufacturer's instructions. NP cells were pre-treated with 100 μ g/mL of PLTs and 100 μ g/mL of PEVs for 24 h, respectively. Then, 400 μ M H₂O₂ were added for 4 h to induce apoptosis in NP cells. NP cells were centrifuged and then

resuspended in 300 mL of PBS supplemented with annexin V–Alexa FITC (5 μ L) and PI (10 μ L). Following incubation (10–15 min, 20 °C) in the dark, cell apoptosis was detected using a flow cytometer after adding 400 μ L 1 \times binding buffer. The total apoptosis rate is the sum of the early stage of apoptosis (Annexin V–positive/PI–negative) and late stage of apoptosis (Annexin V–positive and PI–positive). For apoptosis phenotype, NP cells were labeled with the terminal deoxynucleotidyl transferase-mediated dUTP nick end labeling (TUNEL) Apoptosis Detection Kit (Yeasen, China). The changes in apoptosis levels in the NP cells were detected by fluorescence microscopy, and the TUNEL-positive cells were counted. We analyzed the results using FlowJo software. All experiments were performed with four replicates each.

2.8. Senescence-associated β -gal (SA- β -gal) staining

The senescence phenotype of NP cells was analyzed using SA- β -Gal staining kit (Beyotime, China) and a microscope. Specifically, NP cells were pre-treated with 100 μ M H₂O₂ for 48 h to induce senescence in NP cells. Subsequently, 100 μ g/mL of PLTs and 100 μ g/mL of PEVs were added for 24 h, respectively. NP cells were fixed with 0.2% glutaraldehyde for 15 min at room temperature. Following 3 washes with PBS, NP cells were stained with X-gal staining solution overnight. Blue-stained cells showing high SA- β -gal activity were defined as senescent cells. Representative images were captured under a microscope, and the SA- β -gal-positive cells were counted. All experiments were performed with four replicates each.

2.9. PEVs uptake and mitochondrial localization

The mitochondria of NP cells were labeled with a MitoTracker Green fluorescent probe (Beyotime, China) and cultured in DMEM for 24 h. For uptake studies, the 1'-diiodo-3,3',3'-tetramethylindocarbocyanine perchlorate (DiI) fluorescent probe (Beyotime, China) was incubated with PEVs for 12 h and washed three times with PBS to remove unlabeled particles. DiI-loaded PEVs were incubated with NP cells for 24 h and 4,6-diamidino-2-phenylindole (DAPI) with the NP cell nuclei for 10 min. Then, the cells were fixed with 4% paraformaldehyde. Finally, the localization of DiI and MitoTracker \times Green fluorescent probe was observed using fluorescence microscopy.

2.10. Quantitative real-time polymerase chain reaction (qPCR) analysis

Total RNA was extracted from lysed NP cells using TRIzol reagent (Invitrogen) and an RNA purification kit (CW0581, Kangwei) according to the manufacturer's instructions. The cDNA was reverse transcribed using the MMLV reverse transcription reagent (Takara). β actin was used

as an internal reference. Real-time PCR was performed using a SYBR Master Mix qPCR kit (Takara). The primers used are listed in Table 1. All experiments were performed in triplicate.

2.11. Western blot analysis

Proteins were extracted from the NP cells using a RIPA buffer containing a 1% protease inhibitor (PMSF) (Boster, China). The protein concentration in each group of cells was quantified using a BCA protein concentration kit (Beyotime, China). Proteins were separated using 10% SDS-PAGE and transferred from the gel to a polyvinylidene fluoroether membrane (Millipore, Shanghai, China). The fluoroether membrane was blocked with 5% non-fat milk for 1 h. After blocking, the membrane was washed with Tris-HCl-buffered saline (TBS) containing 0.1% Tween-20 three times for 5 min each. Subsequently, the membranes were incubated with Col2 α , SOX9, Aggrecan, MMP3, MMP13, Adamts5, SIRT1, PGC1 α , TFAM, Nrf1, Nrf2, and β actin at 4 °C for 12 h; the internal control was β actin. The membrane was incubated with a specific horseradish peroxidase-conjugated secondary antibody (Beyotime, China) for 1 h at 18–25 °C after washing with TBST three times for 5 min each. Excess secondary antibody was washed away with TBST three times for 5 min each. Finally, the signal intensity of the reactive bands on the membrane was visualized using the ChemiDoc Touch imaging system (Bio-Rad, USA). All above experiments were performed in triplicate.

2.12. Immunofluorescence staining

Each group of the NP cells was fixed on a control dish with 4% paraformaldehyde for 20 min, washed three times with PBS for 3 times, and the cells were permeabilized with 0.5% Triton X-100 (diluted in PBS) for 20 min. The NP cells were blocked with 5% bovine serum albumin (BSA) for 30 min. Adamts5 (1:100, Proteintech, China), MMP13 (Proteintech, China), Col2 α (1:100; Proteintech, China), Aggrecan (1:100, Sigma, USA), and PGC1 α (1:100, Proteintech, China) were incubated with NP cells at 4 °C for 12 h. Then, the cells were incubated with a fluorescent secondary antibody (goat anti-rabbit Alexa Fluor 488 (1:500, Beyotime, China)) at room temperature for 1 h, which is followed by DAPI for 10 min. Images were obtained using a fluorescence confocal microscope (Nikon, Tokyo, Japan). All above experiments were performed with four replicates each.

2.13. Assessment of mitochondrial function

According to the manufacturer's instructions, the MitoTracker Green (Beyotime, C1048, China), MitoSOX-Red (Beyotime, C1045, China), and JC-1 fluorescent probe (Beyotime, C2006, China) were used to detect

Table 1
Summary of PCR primers used.

Gene Name	Used for	Primer sequence	Product length	Amplicon Size
Col2 α	mRNA quantification	F: CAGGATGCCCGAAAATTAGGG R: ACCACGATCACCTCTGGGT	21 19	132
Sox9	mRNA quantification	F: GAGCCGGATCTGAAGAGGGA R: GCTTGACGTGTGGCTTGITC	20 20	151
Acan	mRNA quantification	F: CCTGCTACTTCATCGACCCC R: AGATGCTGTGACTCGAACCT	20 21	150
Mmp13	mRNA quantification	F: CTTCTTCTTGTGAGCTGGACTC R: CTGTGGAGGTCAGTGTAGACT	23 21	173
Mmp3	mRNA quantification	F: ACATGGAGACTTTTGCCCTTTTG R: TTGGCTGAGTGGTAGAGTCCC	23 21	192
Adamts5	mRNA quantification	F: GGAGCGAGGCCATTTACAAC R: CGTAGACAAGGTAGCCCACTTT	20 22	110
β actin	mRNA quantification	F: CCTCTATGCCAACACAGT R: AGCCACCAATCCACACAG	18 19	230
P16(Cdkn2a)	mRNA quantification	F: GTGTGCATGACGTGCGGG R: GCAGTTCGAATCTGCACCGTAG	18 22	127
P21(Cdkn1a)	mRNA quantification	F: CCAGGCCAAGATGGTGTCTT R: TGAGAAAGGATCAGCCATTGC	20 21	103

mitochondrial membrane potential changes in NP cells. The morphology of mitochondria of NP cells was observed by transmission electron microscopy (TEM; H-9500; Hitachi, Tokyo, Japan). The decrease in mitochondrial membrane potential is a hallmark event in the early stages of apoptosis [76,77]. JC-1 (5,5',6,6'-tetrachloro-1,1',3,3'-tetramethylbenzimidazolylcarbocyanine iodide) is an ideal fluorescent probe widely used to detect mitochondrial membrane potential ($\Delta\Psi_m$). JC-1 monomers can produce green fluorescence ($\Delta\Psi_m\downarrow$) while JC-1 aggregates can produce red fluorescence ($\Delta\Psi_m\uparrow$) [78,79]. We measured the proportion of mitochondrial depolarization by comparing the relative proportions of red and green fluorescence. Therefore, the transition of JC-1 from red fluorescence to green fluorescence can detect the decrease of cell membrane potential and serve as an early detection indicator of apoptosis. Then we used the selective SIRT1 activator (SRT-1720, Beyotime, SC0267) and the selective SIRT1 inhibitor (EX-527, MCE, HY-15452) to verify the mechanism of PEVs repairing impaired mitochondria in pathological NP cells. All experiments were performed with four replicates each.

2.14. ATP detection evaluation

The ATP levels of NP cells were assessed using the luminescent ATP detection assay kit (Abcam, Ab113849). All above experiments were performed with four replicates each.

2.15. Lactic acid detection

According to the manufacturer's instructions, the lactic acid assay kit (Nanjing Jiancheng, A019-2-1) was used to measure the lactic acid concentration in the cell culture serum to reflect the cellular metabolic state. All experiments were performed with four replicates each.

2.16. Manufacture of rat IVDD model

In this study, an IVDD rat model was induced via fine needle puncture. Male Sprague-Dawley rats (200–250 g, 12 weeks old) were randomly allocated into 4 groups (n = 9): NC group, Puncture + vehicle group, Puncture + PLTs group, and Puncture + PEVs group. All rats were treated according to the standard guidelines approved by the Institutional Animal Care and Use Committee of Zhejiang Center of Laboratory Animals. In detail, the rats were anesthetized via the intravenous injection of pentobarbital sodium (40 mg/kg) and then positioned prone on a platform. The IVDD rat models were established using a 26G needle (diameter = 0.45 mm) puncture to coccyx spaces Co7–8. The selected coccygeal intervertebral plane was confirmed using manual palpation and X-ray fluoroscopy. After disinfection with iodate alcohol, a 26G needle was inserted at the level of the annulus fibrosus by palpation, passing through the NP to the contralateral annulus fibrosus. After incomplete penetration, the needle was rotated by 360° twice for 30 s. The depth of needle penetration was controlled by the resistance of contralateral ring fibers. One week after the initial puncture, injured discs injected with 5 μ L vehicle (PBS), 5 μ L PLTs (100 μ g/mL), or 5 μ L PEVs (100 μ g/mL) were set as the vehicle, PLTs, or PEVs group, respectively. Normal IVD Co7–8 was the NC group. Each group of segment treatments was labeled. No deaths or diseases were recorded during the experiment process. After 4 or 8 weeks, the discs were harvested and investigated. All experiments were performed under sterile conditions; the rats were transferred to a warm and ventilated environment after surgery until recovery from anesthesia. Then, the rats were given free access to water and food. The selected coccygeal intervertebral plane was confirmed by digital palpation and fluoroscopy at 4 and 8 weeks after the first surgery.

2.17. Radiological assessment analysis

The micro-computed tomography (micro-CT, Skyscan1275) and

magnetic resonance imaging (MRI) were performed at 4- and 8-weeks post-operation with a GE Sigma CV/I (1.5 T) to evaluate changes in the NP signal and height of the intervertebral space. Image J software was used to measure the signal intensity of the IVD at Co7-8 on T2-weighted central images. According to the modified Thomson classification, the MRI images are classified into grades I to IV (I, normal; II, signal intensity is slightly decreased but the high signal area is significantly narrowed; III, signal intensity is moderately decreased; and IV, signal intensity is severely decreased); they were evaluated by three experienced radiologists and three orthopedic surgeons. Further, the IVD height was measured by micro-CT analysis and calculated as the disc height index (DHI) that represents the average height of the anterior, middle, and posterior discs. The change in the DHI was calculated using the value at 0 week as a reference. The CT images were measured using Data-viewer software, and DHI was calculated using the following equation: disc height index (DHI) = $2 \times (A + B + C) / (D + E + F + G + H + I)$; DHI% = measured DHI/NC group DHI \times 100% for each group).

2.18. Histological analysis and immunofluorescence staining

The Digital Pathology Slide Scanner (KFBIO) were performed at rats intervertebral disc (IVD). The IVD tissues were stripped from the IVD segments of the rats. The IVDs were fixed in 4% buffered paraformaldehyde and decalcified in a decalcification solution (14% EDTA) at 18–25 °C for 4 weeks. The decalcified discs were paraffin-embedded to obtain sections; the sections were then stained with hematoxylin and eosin (H&E), Alcian blue (A&B), Safranin O-fast Green (S&O), and Sirius Red (S&R). The specimens were examined and photographed using a digital microscope (KFBIO, KF-PRO-120). According to the definition of histological grade (Table 2), the histological images of each group are classified into 0 to 15 scores. For immunofluorescence staining, discs were blocked by incubation with 5% BSA (Fdbio science); incubated with primary antibodies against Col2 α , MMP13, and PGC1 α ; and this was followed by incubation with the corresponding secondary antibodies conjugated with Alexa Fluor 488 fluorescent dye (Proteintech) and stained with DAPI (Beyotime). Discs were blocked by incubation with 5% BSA (FDbio Science), followed by incubation with the DHE fluorescence and MitiSOX Red fluorescence probes and staining with DAPI (Beyotime). The morphology of mitochondria of IVD was observed by transmission electron microscopy (TEM; H-9500; Hitachi, Tokyo, Japan). All experiments were performed with three replicates each.

Table 2
Definition of histological grade.

Category	Grade
I. Matrix of the nucleus pulposus	1. Normal gelatinous appearance
	2. Slight condensation of the extracellular matrix
	3. Moderate/severe condensation of the extracellular matrix.
II. Cellularity of the nucleus pulposus	1. Normal cellularity with large vacuoles in the gelatinous structure of the matrix
	2. Slight decrease in the number of cells and fewer vacuoles
	3. Moderate/severe decrease (>50%) in the number of cells and no vacuoles
III. Structure of anulus fibrosus	1. Normal, pattern of fibrocartilage lamellae without ruptured fibers and without a serpentine appearance anywhere within the anulus.
	2. Slight ruptured or serpentine patterned fibers (<30%)
	3. Moderate/severe ruptured or serpentine patterned fibers (>30%).
IV. Border between the nucleus pulposus and anulus fibrosus	1. Normal
	2. Minimally interrupted
	3. Moderate/severe interruption.

2.19. Systemic toxicity experiments in vivo

After rats were sacrificed, the main organs (heart, liver, spleen, lung, and kidney) were collected for H&E staining to evaluate systematic pathological changes.

2.20. Statistical analysis

All study results are presented as the mean \pm standard deviation (SD). Statistical analyses were performed using GraphPad Prism (v5.0) to perform one-way or two-way analysis of variance (ANOVA). Duplicate groups were included in all experiments. The differences between the groups were further assessed using Tukey's multiple comparison test. The difference in the results was significant when the p-value was <0.05 . The significance of these numbers is indicated by asterisks: * $p < 0.05$, ** $p < 0.01$, *** $p < 0.005$, and **** $p < 0.001$. All signal intensity and fluorescence expression levels were quantified using ImageJ software.

3. Results

3.1. PEVs preparation and characterization

PEVs were obtained from PLTs through extrusion method (extrusion through 1000, 500, and 200 nm filters) (Fig. 1A) and were injected into the intervertebral disc of rats (Fig. 1B). A previous study reported that cells can release a large number of cell-derived extracellular vesicles (CEVs) in a short period of time through mechanical extrusion [80–83]. The technical theory of the method is that CEVs are formed as a result of the disruption of the cell membrane using shear or frictional forces and the reorganization of lipid bilayer-forming vesicles in seconds [80,84]. Meanwhile, vesicles can randomly encapsulate surrounding cellular components or drugs during the extrusion process; thus, part of the unencapsulated protein or components would be lost [85]. Then we drew the schematic diagram of the preparation and injection of PEVs (Fig. 2A). In this study, we compared the properties of PLTs and PEVs using cryo-TEM. The PEVs have a smaller size of ~ 200 nm compared with PLTs with a size of $\sim 1 \mu\text{m}$ (Fig. 2B). Then, we measure PEVs and PLTs using DLS, and the results show that PLTs have a particle size of $1.1 \mu\text{m}$ and a zeta potential of -22.8 mV, whereas the PEVs have a particle size of 195.6 nm and a zeta potential of -4.3 mV (Fig. 2C). Subsequently, we place PEVs and PLTs at 37°C for 1, 3, 5, and 7 days and find that the size of PEVs remained stable during this period using DLS; the size of the PLTs gradually decrease (Fig. 2D). We then examine the proliferative effect of PEVs on NP cells using the CCK-8 kit. The results of CCK-8 depicted that the most suitable concentration of PEVs to promote NP cell proliferation is $100 \mu\text{g}/\text{mL}$ (Fig. 2E). We selected $100 \mu\text{g}/\text{mL}$ PEVs and $100 \mu\text{g}/\text{mL}$ PLTs in the subsequent cellular experiment. The cell proliferation assay elucidated that NP cells had a good proliferative capability after PEVs treatment. In addition, no apparent biological toxicity was examined in all groups at rats after administration of PEVs and PLTs after 4 and 8 weeks (SI Fig. 2), which was consistent with the outcome of CCK-8 assay.

Furthermore, we determined the protein composition of PLTs and PEVs to study the reasons for this result, and we found that their compositions are similar in the Coomassie Brilliant Blue staining (Fig. 2F). The membrane marker proteins (CD9, CD41, and CD63) were significantly enriched in PEVs, and cytoplasmic proteins of PLTs (GAPDH and β actin) were lower in PEVs (Fig. 2G).

Then we compared the abilities of PLTs and PEVs to produce inflammatory cytokines following thrombin activation. We observed a significant increase in IL-1 β , IL-6, and TNF α production in platelets after thrombin addition. In contrast to PLTs, PEVs exhibit no significant changes in inflammatory factor levels before and after thrombin addition (Fig. 2H). The results indicate that activated platelets can accelerate inflammation through the release of inflammatory factors (IL-1 β , IL-6, and TNF α); by contrast, PEVs do not release these pro-inflammatory factors to aggravate inflammation, thus making them a more promising

option for targeting inflammatory diseases. The reason why PEVs do not cause inflammation may be that their cytoplasmic proteins are reduced and the pathways for releasing inflammatory factors are disturbed. Referring to a previous study, the low level of cytokine releases from PEVs may be attributed to the fact that α -granules (particle size ranging between 200 and 300 nm) do not exist in PEVs [39,86].

3.2. PEVs alleviate oxidative stress in NP cells

We used DCFH-DA as a probe to assess ROS levels in untreated NP cells (control group), H_2O_2 pretreated NP cells (H_2O_2 group), $100 \mu\text{g}/\text{mL}$ platelet-treated NP cells (PLTs group), and $100 \mu\text{g}/\text{mL}$ platelet vesicle-treated NP cells (PEVs group). Fig. 3A and B depicted that there is a low ROS level in the control group, whereas a high ROS level elucidated that strong green fluorescence can be clearly observed after H_2O_2 stimulation. The addition of PLTs resulted in a decrease in cellular fluorescence intensity. Interestingly, the effect of PEVs on reducing ROS levels was more pronounced than that of PLTs. These results indicate that PEVs have a better ability to scavenge intracellular ROS. Further, we quantified H_2O_2 -induced ROS production by flow cytometry. The percentages of DCF-positive NP cells were 6.9%, 38.25%, 27.65%, and 16.25% in the control, H_2O_2 , PLTs, and PEVs groups, respectively (Fig. 3C and D). Together, these results suggest that PEVs have a better antioxidant capacity than that of PLTs.

3.3. PEVs inhibit apoptosis and senescence in NP cells

We utilized the methods of FITC-annexin V/PI apoptosis assay, TUNEL staining, SA- β -Gal staining, and P16 and P21 mRNA detection to verify the effect of PEVs on the apoptosis and senescence phenotype of NP cells. The flow cytometry results of the PI/FITC apoptosis assay yielded apoptosis rates of NP cells of 5.7%, 55.7%, 41.69%, and 17.21% in the NC, H_2O_2 , PLTs, and PEVs groups, respectively (Fig. 3E and F). The results of TUNEL staining depicted a low apoptosis rate in the NC group, whereas a strong, clearly observable green fluorescence of H_2O_2 group elucidated a high apoptosis rate. The addition of PEVs and PLTs resulted in a decrease in cellular fluorescence intensity. PEVs exerted superior reducing effect on the apoptosis rate of NP cells compared with PLTs (Fig. 3G and H). Taken together, these data indicate that PEVs inhibit the apoptosis of NP cells. Regarding the result of Sa- β -Gal staining, the senescence of NP cells started to be considerably reduced by the action of PEVs, whereas the effect of PLTs was not significant (Fig. 3I and J). Additionally, the qPCR results illustrated that H_2O_2 stimulation increases the mRNA expression levels of cell senescence markers (P16, P21), whereas PEVs notably downregulated them (Fig. 3K). These data indicate that PEVs inhibit senescence in NP cells. Mitochondrial dysfunction is an essential part of the senescence and apoptosis phenotype, which is linked with the major building blocks of senescence and apoptosis via multiple feedback loops [87–90]. Because PEVs contain mitochondria-related proteins such as sirtuin-1 (SIRT1), we suppose that PEVs may inhibit senescence and apoptosis in NP cells by regulating mitochondrial function.

3.4. Effect of PEVs on the metabolism proteins of NP cells

We examined the expression of genes related to ECM synthesis and degradation using qPCR to study the effect of PEVs on the metabolism of NP cells. The results illustrated that H_2O_2 stimulation increased the expression of catabolic genes (*Mmp3*, *Mmp13*, and *Adams5*) and decreased the expression of anabolic genes (*Col2a*, *Sox9*, and *Acan*). After PEVs treatment, the expression of catabolic genes in the NP cells is downregulated and that of anabolic genes is upregulated (Fig. 4A and B). Then, we examined the protein levels involved in cell anabolism and catabolism using western blotting. Considering the mRNA expression data, the PEVs increased anabolic protein (*Col2a*, *Sox9*, and *Aggrecan*) levels and reduced catabolic protein (*MMP3*, *MMP13*, and *ADAMTS5*)

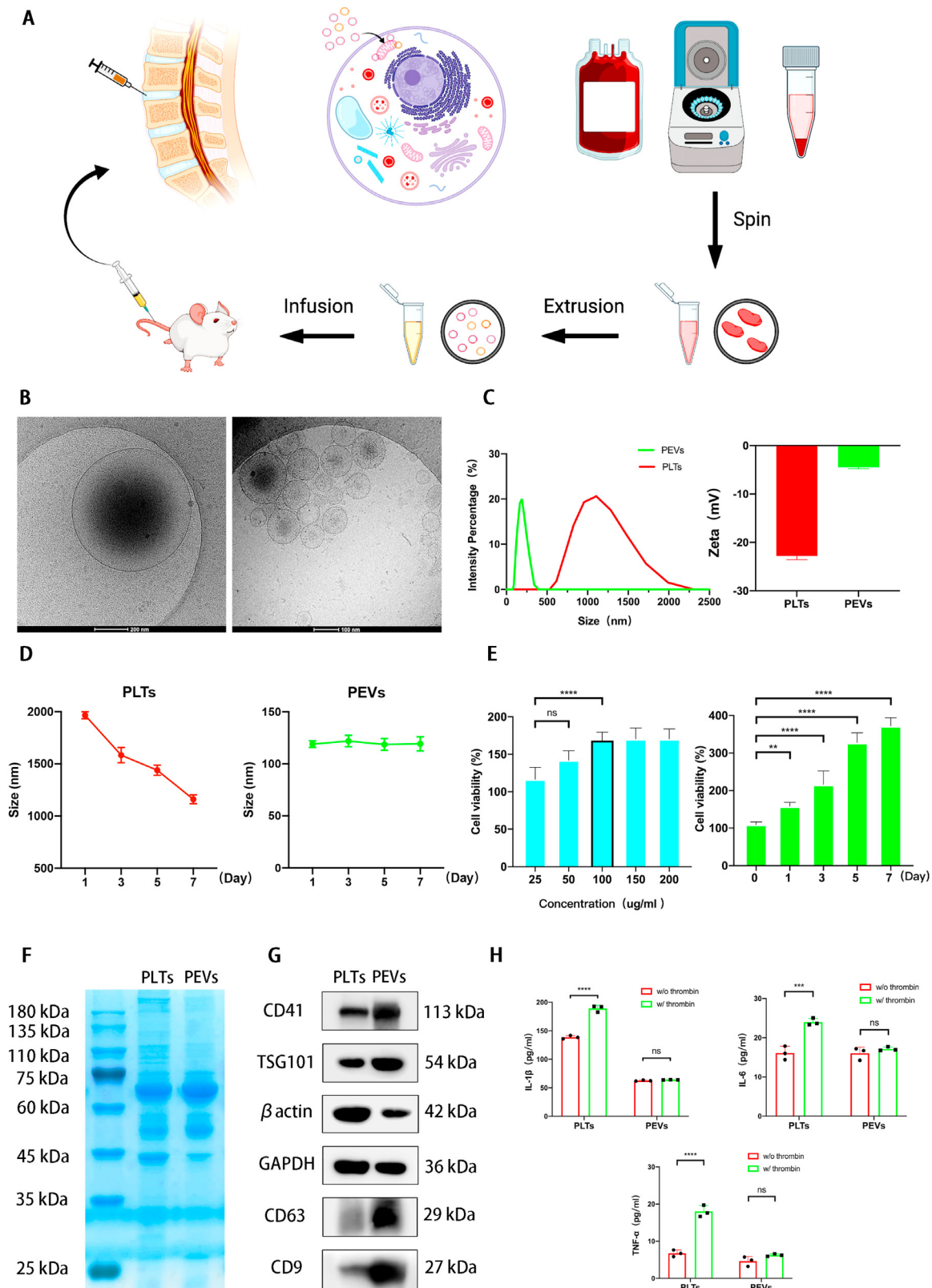


Fig. 2. Preparation and characterization of the platelet-derived extracellular vesicles. (A) Schematic diagram of the preparation and injection of PEVs. (B) Cryo-TEM images of PLTs and PEVs. Scale bar = 200 nm, 100 nm. (C) The size distribution analysis and surface zeta potential of PLTs and PEVs. (D) Stability of PLTs and PEVs *in vitro*. (E) The toxicity of different concentrations (0–200 µg/mL) and durations (0–7 days) of 100 µg/mL PEVs in NP cells by CCK-8 kit assay. (F) SDS-PAGE of PLTs and PEVs with Coomassie brilliant blue staining. (G) Western blot analysis of CD41, TSG101, βactin, GAPDH, CD63, and CD9 from the PLT and PEV lysates. Quantification of CD41 protein is in [SI Fig. 3](#). Uncropped gel is in [SI Fig. 4A](#). (H) The amount of IL-1β, IL-6, and TNFα cytokines from PLTs and PEVs in the absence and presence of thrombin. The significance between every two groups was calculated using a two-tailed Student's t-test (H) or one-way analysis of variance (ANOVA) with Tukey's post-hoc test (D–E). Data are presented as mean ± SD (n = 3). (Scale bars are listed above; *: P < 0.05, **: P < 0.01, ***: P < 0.005, and ****: P < 0.001).

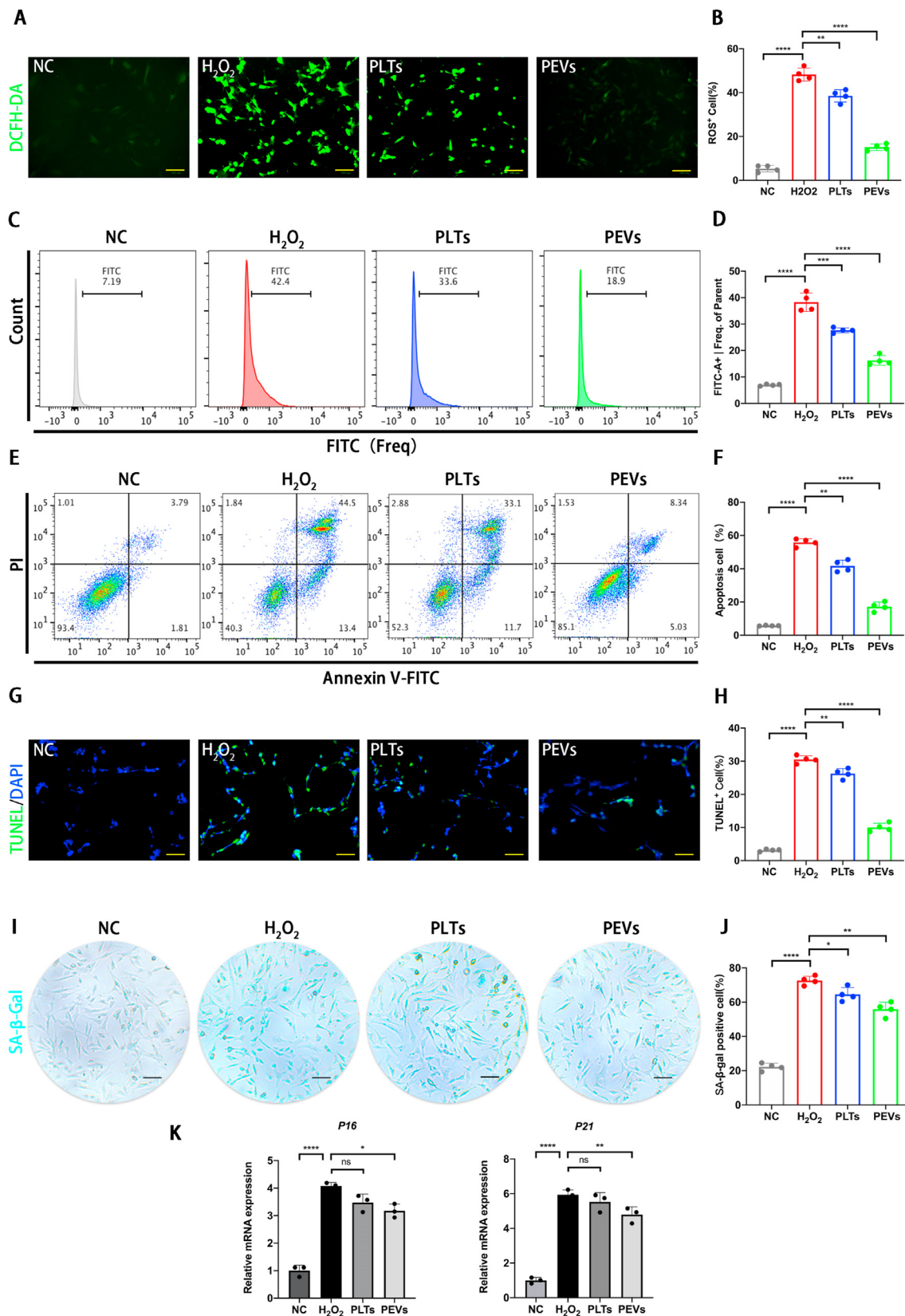


Fig. 3. Effects of PEVs on oxidative stress, apoptosis, and senescence in degenerative NP cells. (A) Fluorescence images of NP cells with ROS staining by DCFH-DA probe. Scale bars = 50 μ m. (B) ROS level of NP cells according to (A). (C) The ROS level was determined by flow cytometry with DCFH-DA probe. (D) The ROS abundance of NP cells according to (C). (E–F) Detection of NP cells apoptosis by flow cytometry. (G–H) Detection of NP cells apoptosis by fluorescence confocal microscopy. Scale bars = 50 μ m. (I–J) NP cells senescence detection by SA- β -gal staining. Scale bars = 50 μ m. (K) The effects of PLTs and PEVs on mRNA expression levels of P16 and P21 in NP cells subjected to 100 μ M H₂O₂ stimulation. Significance between four groups was calculated using one-way ANOVA with Tukey's post-hoc test. Data are presented as mean \pm SD (n = 4). (Scale bars are listed above; *: P < 0.05, **: P < 0.01, ***: P < 0.005, and ****: P < 0.001).

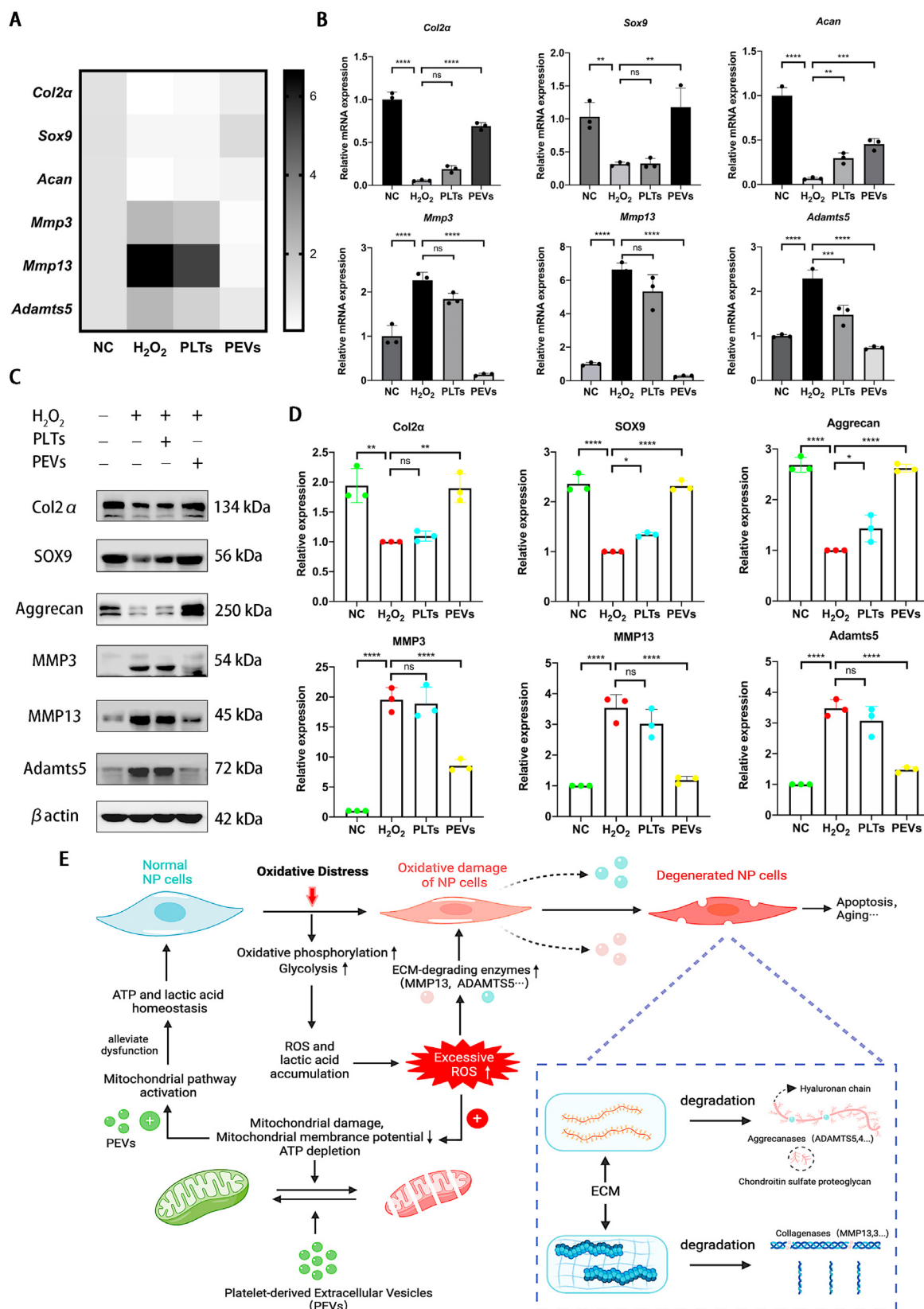


Fig. 4. PEVs regulate metabolism proteins in degenerative NP cells. (A–B) The effects of PLTs and PEVs on mRNA expression levels of Col2 α , Sox9, Acan, Mmp3, Mmp13, and Adamts5 with 200 μ M H₂O₂ stimulation. (C) Western blot analysis showing Col2 α , Sox9, Aggrecan, MMP3, MMP13, and ADAMTS5 protein levels after treatment with 100 μ g/mL PEVs (with 200 μ M H₂O₂ stimulation) and 100 μ g/mL PLTs. β actin was used as a loading control. Uncropped gel is in SI Fig. 4B. (D) Quantitative analysis of metabolism protein expression differences in each group. (E) The schematic of PEVs regulating metabolism proteins in degenerative NP cells by repairing damaged mitochondria and regulating ECM-degrading enzymes. Significance between four groups was calculated using one-way ANOVA with Tukey's post-hoc test. Data are presented as mean \pm SD (n = 3). (Scale bars are listed above; *: P < 0.05, **: P < 0.01, ***: P < 0.005, and ****: P < 0.001).

levels in H₂O₂-stimulated NP cells (Fig. 4C and D). According to the result and reference [91], we draw a schematic of the effect of PEVs in NP cells by repairing damaged mitochondria and regulating ECM-degrading enzymes (Fig. 4E). The immunofluorescence confirmed that PEVs enhanced the fluorescence intensities of Col2 α and Aggrecan and attenuated the fluorescence intensities of ADAMTS5 and MMP13 in H₂O₂-stimulated NP cells (Fig. 5A and B). The results indicate that PEVs can enhance cellular anabolism and attenuate cellular catabolism in pathological NP cells.

3.5. PEVs uptake and mitochondrial colocalization

We first labeled the mitochondria of NP cells with a MitoTracker Green probe to test the ability of NP cells to take up PEVs. Then, we labeled the PEVs with a DiI membrane probe. Finally, we incubated the labeled NP cells with PEVs (Fig. 6A). The confocal microscopy pictures a partial overlap of DiI and MitoTracker Green fluorescence, and this indicates that PEVs can co-localize with the mitochondria of NP cells after being endocytosed by NP cells (Fig. 6B). Subsequently, we drew a figure of distribution of PEVs (Red) and NP cells (Green) using Image J software. Fig. 6C illustrated PEVs colocalized with mitochondria. Then, we validated the endocytic pathway of PEVs in NP cells using chlorpromazine, filipin III, wortmannin, and cytochalasin D to inhibit clathrin-mediated endocytosis, caveolae-mediated endocytosis, micropinocytosis, and actin-mediated endocytosis, respectively. We used DiI to label PEVs and DiO to label NP cells. According to flow cytometry, the percentage of DiI/DiO-positive NP cells is 38.20%, 36.40%, 35.05%, 16.32%, 30.95%, and 1.02% in the control, chlorpromazine, filipin III, cytochalasin D, wortmannin, and 4 °C groups, respectively (Fig. 6D and E). The results showed that the cellular uptake of PEVs was suppressed at 4 °C by cytochalasin D or by wortmannin, but not by Filipin III or chlorpromazine. Therefore, the uptake of PEVs with diameters of 100–200 nm by NP cells is mediated by actin-mediated endocytosis. Further, a small number of PEVs are endocytosed by micropinocytosis because of their larger size. The previous study demonstrated that chlorpromazine, filipin III, wortmannin, and cytochalasin D are toxic [92]. To obtain CCK-8 results, the chosen concentrations were 25, 3, 5, and 5 μ M for chlorpromazine, filipin III, wortmannin, and cytochalasin D, respectively.

3.6. Effects of PEVs on mitochondrial function of cells *in vitro*

We detected the abundance of PGC1 α (a regulator of mitochondrial genesis) in NP cells using immunofluorescence staining to confirm that PEVs could restore mitochondrial function in degenerated NP cells. The results illustrated that the H₂O₂ stimulation significantly downregulated the abundance of PGC1 α , whereas the treatment of PEVs restored the abundance of PGC1 α (Fig. 7A and B). Treatment with PLTs resulted in only slight upregulation of PGC1 α . Studies have suggested that the activation of AMPK can promote the expression of SIRT1, PGC1 α , and TFAM, which can help maintain mitochondrial function in cells [58]. Then, we examined the levels of these mitochondria-related proteins (SIRT1, PGC1 α , TFAM, Nrf1, and Nrf2) by western blotting. The results elucidated that these proteins were downregulated following H₂O₂ stimulation (Fig. 7C and D). In contrast, PLTs and PEVs increased the abundance of these proteins, and the PEV treatment was more effective than the PLTs treatment. Next, we used MitoSOX Red staining to observe the effect of PEVs on mitochondrial ROS levels. MitoSOX Red staining results showed low ROS level in the mitochondria of the NC group and significantly increased levels in the H₂O₂ group (Fig. 7E and F). The ROS level of PEVs group was significantly lower than those in the H₂O₂ and PLTs groups. These data indicate that PEVs can reduce mitochondrial ROS levels in NP cells.

We evaluated the mitochondrial mass and mitochondrial membrane potential ($\Delta\Psi$ m) of NP cells after PEVs treatment to further investigate the effect of PEVs on mitochondrial function. Compared with the H₂O₂ group, PEV-treated NP cells showed enhanced mitochondrial mass, as

depicted by the increased MitoTracker Green staining (Fig. 8A and B). Furthermore, decreased $\Delta\Psi$ m is a hallmark event of cellular oxidative stress in early apoptosis, and it can be easily detected by the transformation of JC-1 from red to green fluorescence [78]. Normal NP cells emit strong red and weak green fluorescence using the JC-1 probe and indicate a higher $\Delta\Psi$ m (Fig. 8C and D). After H₂O₂ stimulation, the green fluorescence started to increase, and the red fluorescence diminished, which indicate a lower $\Delta\Psi$ m. We found a significant increase in red fluorescence and a decrease in green fluorescence in the PEVs group, which indicates an increased $\Delta\Psi$ m. These results suggest that PEVs can attenuate oxidative stress-induced mitochondrial dysfunction in NP cells.

We further detected the content of lactic acid and ATP produced by NP cells under H₂O₂ stimulation to further observe mitochondrial function of cells. The increase in the lactic acid induced by H₂O₂ stimulation reflected an elevated level of glycolysis as the main product of the glycolysis; this was attenuated by PEVs treatment (Fig. 8E). In addition, the ATP concentration of NP cells decreased after H₂O₂ stimulation. Interestingly, this concentration increases in PEVs group (Fig. 8F). In conclusion, PEVs can correct the mitochondrial dysfunction in H₂O₂-treated NP cells.

Then, we observed the mitochondrial morphology of NP cells by TEM and quantified the percentage of mitochondrial vacuoles (Fig. 8G). The TEM results revealed that the percentage of mitochondrial vacuoles/mitochondria in the PEVs group is markedly lower than those in the H₂O₂ and PLTs groups. These data suggested that PEVs can restore mitochondrial function in NP cells. Therefore, we considered the supplement of mitochondrial related proteins by PEVs results in restoring the mitochondrial function of NP cells.

3.7. Proteomic analysis

We evaluated PEVs and PLTs using proteomics to further clarify the reasons for the therapeutic effects of PEVs. The results showed that the PEVs contained 1732 PLTs parental proteins. Compared with PLTs, there are 790 upregulated proteins and 942 downregulated proteins (Fig. 9A). Through GO enrichment analysis, we classify these parental proteins into biological processes, molecular functions, and cellular components (Fig. 9B). The proteomic analysis elucidated that the proteins in PEVs are derived from the cytosol (1085), extracellular exosome (854), plasma membrane (678), nucleoplasm (444), and mitochondrion (318) (Fig. 9C). The GO biological process analysis revealed that 17.26% of PEVs proteins are involved in metabolic processes, 3.47% in vesicle-mediated transport, 2.8% in mitochondrial electron transport, and 2.14% in mitochondrial ATP synthesis biological processes (Fig. 9D). The GO molecular functional analysis revealed that these components are involved in the binding of specific proteins, ATP, ATPase, actin, and platelet-derived growth factor receptors, and this can contribute to the phagocytosis and localization of PEVs by NP cells (Fig. 9E). Next, the mitochondrial protein contents of PEVs are similar with PLTs (Fig. 9F), which suggests that PEVs retain the mitochondrial components of platelets. In addition, PEVs and PLTs contained SIRT1 proteins (P48047), which can play an essential role in the protection of mitochondrial function both *in vitro* and *in vivo*. Compared with PLTs, PEVs retain partial mitochondrial ATP and ROS proteins (Fig. 9G). Moreover, enrichment analysis illustrated that different parts of mitochondria were enriched in PEVs, including mitochondria, mitochondrial inner membrane, mitochondrial complex, mitochondrial matrix, mitochondrial intermembrane space, mitochondrial outer membrane, and mitochondrial nucleoid (Fig. 9H). These results suggest that PEVs may repair impaired mitochondria by replenishing mitochondria-related proteins after endocytosis by NP cells, which can restore the mitochondrial function of NP cells. The data helped our follow-up focus on investigating the role of SIRT1 in NP cells, as further demonstrated by PEVs restoring mitochondrial function in NP cells.

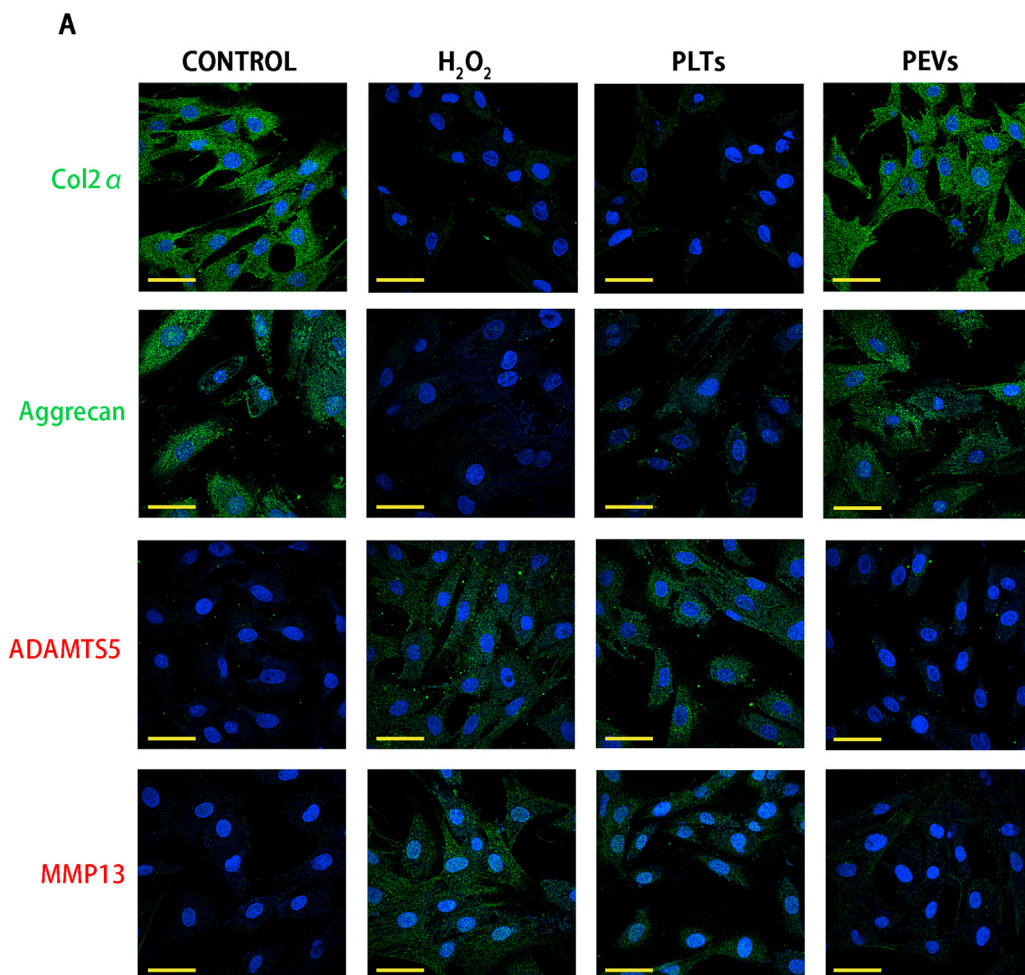
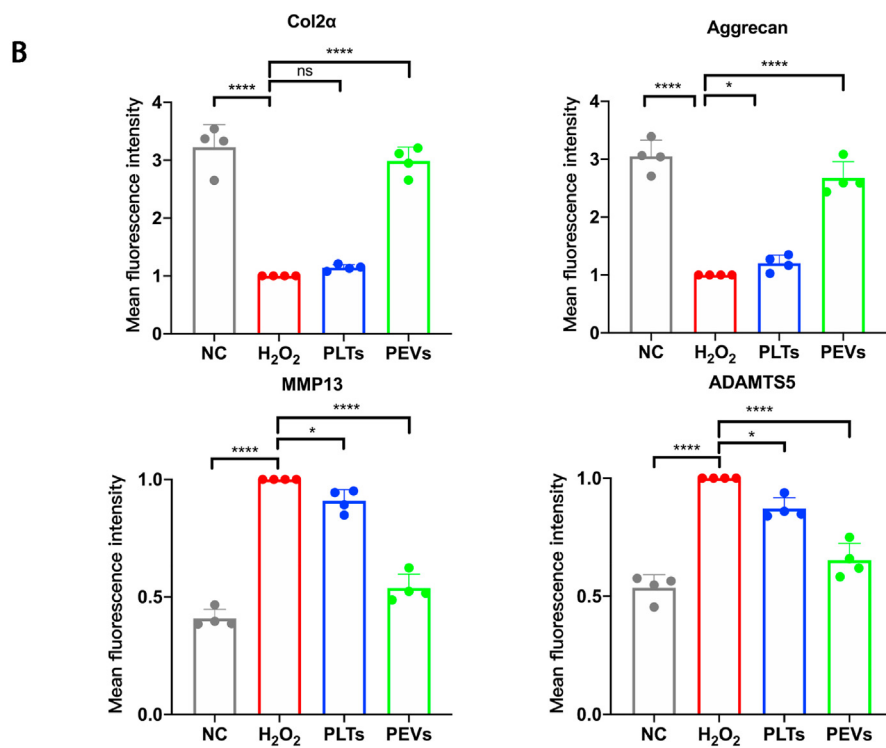
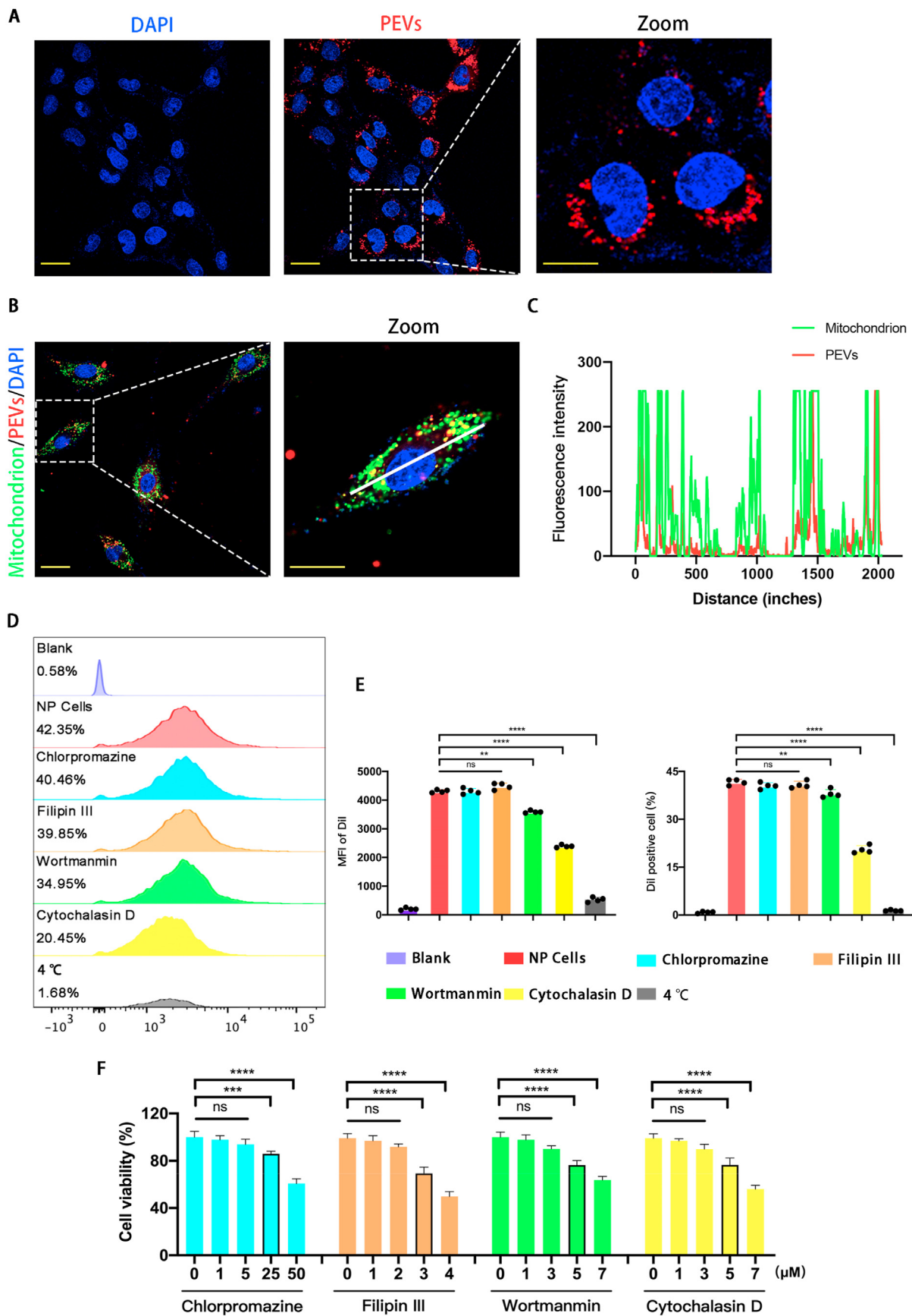


Fig. 5. Effects of PEVs on metabolic proteins of NP cells. (A) Immunofluorescence assay was performed to assess expression of Col2α, Aggrecan, ADAMTS5, and MMP13. Scale bars = 50 μm. (B) Quantification of specific immunofluorescence intensities according to (A). Significance between four groups was calculated using one-way ANOVA with Tukey's post-hoc test. Data are presented as mean ± SD (n = 4). (Scale bars are listed above; *: P < 0.05, **: P < 0.01, ***: P < 0.005, and ****: P < 0.001).





(caption on next page)

Fig. 6. PEVs uptake and mitochondrial colocalization. (A) Fluorescence confocal microscopy image of PEVs uptake. Scale bar = 50 μm . (B–C) Fluorescence confocal microscopy images and line-scanning profiles of NP cells mitochondria colocalized with PEVs. Red: PEVs, Green: mitochondria, Blue: DAPI-labeled nuclei. Scale bar = 50 μm . (D) NP cells measured by flow cytometry after cells were pretreated with each inhibitor (chlorpromazine, filipin III, wortmannin, and cytochalasin D) for 0.5 h and cultured with PEVs for 24 h at 37 °C or at 4 °C. (E) Quantification of specific Immunofluorescence intensities (MFI) and the percentage of Dil positive cells by flow cytometry. (F) The toxicity of different concentration of each inhibitor (chlorpromazine, filipin III, wortmannin, and cytochalasin D) in NP cells by CCK-8 kit assay. Significance between six groups was calculated using one-way ANOVA with Tukey's post-hoc test. Data are presented as mean \pm SD (n = 4). (Scale bars are listed above; *, $P < 0.05$, **, $P < 0.01$, ***, $P < 0.005$, and ****, $P < 0.001$).

3.8. Effects of inhibitor and activator on pathological NP cells

According to the result of immunofluorescence staining, PGC1 α was present at a low protein level in pathological NP cells (H_2O_2 group), and its fluorescence intensity almost disappeared after the addition of the selective SIRT1 inhibitor (H_2O_2 +EX-527 group). Compared with the H_2O_2 +EX-527 group, the H_2O_2 +EX-527+PEVs group exhibited elevated protein levels of PGC1 α , while the H_2O_2 +PEVs group showed a significant increase in PGC1 α protein abundance (Fig. 10A and B). The Western blot analysis results indicated that the mitochondria-related protein abundances of PGC1 α and TFAM were lower in the H_2O_2 +EX-527 group compared with those in the H_2O_2 group (Fig. 10C and D). Compared with those in the H_2O_2 +EX-527 group, the proteins in the H_2O_2 +PEVs group were effectively increased. Then, we examined the abundances of the mitochondria-related proteins PGC1 α and TFAM with the addition of the SIRT1 activator (Fig. 10E and F). The results indicate that these proteins are upregulated following SRT-1720 stimulation (H_2O_2 +SRT-1720 group). Moreover, the mitochondria-related protein abundances were increased significantly in the H_2O_2 +SRT-1720+PEVs group. The result of PGC1 α immunofluorescence staining illustrated that SRT-1720 stimulation significantly upregulated the abundance of PGC1 α , whereas the effect of treatment of PEVs was same as that of SRT-1720 (Fig. 10G and H). Treatment with SRT-1720 and PEVs (H_2O_2 +SRT-1720+PEVs group) resulted in a significant upregulation of PGC1 α . Taken together, the data demonstrate that PEVs restoring mitochondrial function in pathological NP cells by activating the SIRT1–PGC1 α –TFAM pathway via SIRT1 supplementation.

3.9. Effects of rotenone on PEVs-treated pathological NP cells

We used rotenone to suppress electron transport in the mitochondria to verify that PEVs exerted a therapeutic effect on cells by repairing mitochondria. The protein level of PGC1 α was low in pathological NP cells (H_2O_2 group), and the fluorescence intensity of PGC1 α diminished to almost zero after the addition of rotenone (H_2O_2 +rotenone group). Although the H_2O_2 +PEVs group exhibit the elevated protein levels of PGC1 α compared with the H_2O_2 group, the H_2O_2 +PEVs + rotenone group showed a significant decrease in PGC1 α protein abundance compared with the H_2O_2 +PEVs group (Fig. 11A and B). The results of western blotting revealed that the mitochondria-related protein abundances of SIRT1, PGC1 α , and TFAM were decreased in the H_2O_2 +rotenone group compared with those in the H_2O_2 group (Fig. 11C and D). In contrast, these proteins were effectively increased in the H_2O_2 +PEVs group compared to the H_2O_2 group. However, rotenone significantly inhibited the elevating effect of PEVs on these proteins. Further, the effect of PEVs on the mitochondrial function (lactic acid and ATP) of pathological NP cells was tested; the concentration of lactic acid decreased in H_2O_2 +PEVs group compared with H_2O_2 +PEVs + Rotenone group (Fig. 11E), and the ATP concentration increased in H_2O_2 +PEVs group compared with H_2O_2 +PEVs + Rotenone group (Fig. 11F). These data indicated that H_2O_2 -induced cellular was mitochondrial function inhibited by rotenone, and the therapeutic effect of PEVs protected mitochondrion of NP cells by alleviating the oxidative stress damage.

3.10. PEVs retard disc degeneration in the rat IVDD model

We hypothesized that PEVs could be an effective strategy to treat IVDD because PEVs could restore the mitochondrial function of NP cells

in vitro. To this end, we established a rat IVDD model by needle puncture of the rat caudal IVD. First, we confirmed the selected caudal intervertebral plane for puncture using manual palpation and X-ray fluoroscopy (Fig. 12A). Second, we injected the PEVs and PLTs into the IVD. Finally, the IVD disc height and index of the CT images are measured and calculated, respectively (Fig. 12B). Repair of the nucleus pulposus (NP) was observed by magnetic resonance imaging (MRI). At 4 and 8 weeks, the NC group showed a high T2-weighted signal, which indicated high water content in the NP by measuring the signal intensity of NP (Fig. 12C). The vehicle group showed a progressively lower T2-weighted signal. Compared to the vehicle group, the PEVs group showed a relatively stable T2-weighted signal at 4 and 8 weeks after injection, whereas the PLTs group showed a significant lower in the signal. Statistical analysis results indicated significant difference in T2-weighted signal between the PEVs and vehicle groups at 4 and 8 weeks (Fig. 12D); meanwhile, no significant difference was observed between the signals of the PLTs and vehicle groups. These results demonstrated that PEVs can alleviate the inflammatory microenvironment to retard IVDD and restore the water content of NP, whereas PLTs do not exert a significant effect. Subsequently, we used microcomputed tomography (micro-CT) and disc height index (DHI) analyses to assess disc space height (Fig. 12E). Throughout the time course, no significant change in the intervertebral space height was observed in the NC group. At 4 and 8 weeks, the IVD height of rats in the vehicle and PLTs groups started to decrease, whereas this phenomenon was not apparent in the PEV group. The statistical results of micro-CT were similar to those of MRI (Fig. 12F), and these data indicated that PEVs can maintain the stability of the IVD and retard the development of IVDD.

Then we stain IVD from 4- and 8-weeks rats with H&E, A&B, and S&O (Fig. 13A, B, C). The NC group exhibited a normal gel-like appearance of the NP, normal morphology of the fibrocartilage, no AF breakage, no serpentine appearance within the AF, and a clear border between the NP and the AF. However, the Vehicle and PLTs groups showed gradual NP atrophy and AF breakage at 4 and 8 weeks. The structure and NP content of the IVD in the PEVs group were significantly repaired compared to the Vehicle and PLTs groups. S&R staining revealed that the IVD height was obviously reduced in the Vehicle group at 4–8 weeks; the AF was severely broken, and the NP was replaced by AF (Fig. 13D). In contrast, the PEVs group showed a normal appearance of AF and a clear boundary between the NP and AF regions. The histological grade results suggest that intact NP tissue is observed in the NC group at 4 and 8 weeks (Fig. 13E and F). The Vehicle group exhibited severely degenerated NP tissue with a narrowing of the IVD height. The PLTs group showed moderately degenerated NP tissue; the PEVs group promoted NP tissue repair and IVD height restoration. These data indicate that PEVs can retard IVDD *in vivo*.

3.11. Effects of PEVs on the mitochondrial function of IVD *in vivo*

The IVDD tissues are characterized by a loss of ECM and the high expression of matrix-degrading enzymes such as matrix metalloproteinases (MMPs). We used the immunofluorescence to detect Col2 α and MMP13 expression in the different groups. Compared to the NC group, the Vehicle and PLTs groups showed significantly lower Col2 α levels (Fig. 14A and B). The PEVs treatment significantly elevated Col2 α levels compared to the Vehicle and PLTs groups. Meanwhile, the fluorescence intensity of MMP13 was significantly higher in the Vehicle and PLTs groups compared with that for the NC group (Fig. 14C and D). In contrast, PEVs dramatically reduced the fluorescence intensity of MMP13

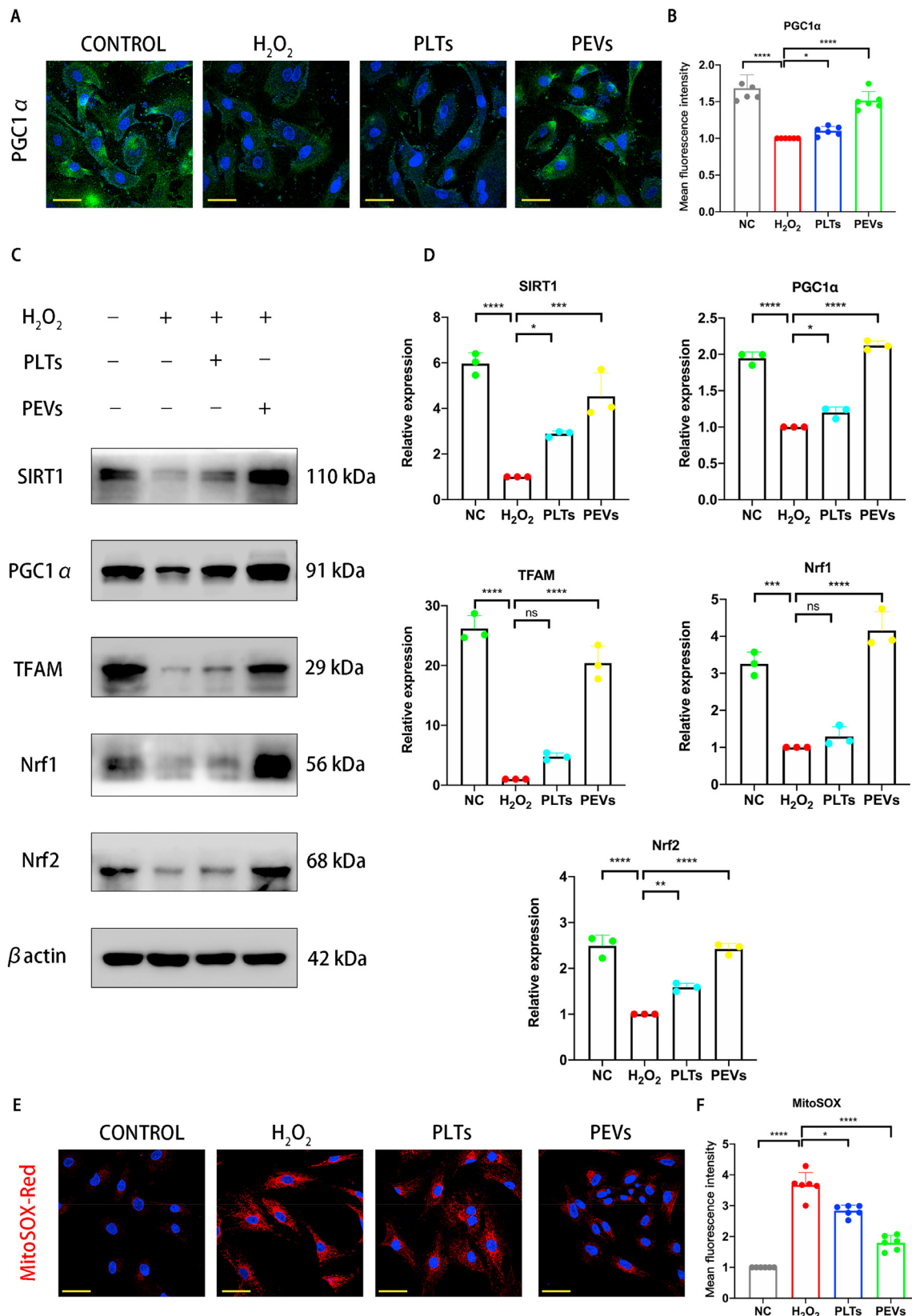


Fig. 7. Effects of PEVs on mitochondrial functional proteins. (A) Fluorescence expression of mitochondrial functional protein PGC1 α . Scale bar = 50 μ m. (B) Quantification of specific immunofluorescence intensities according to (A). (C) Western blot analysis showing SIRT1, PGC1 α , TFAM, Nrf1, and Nrf2 protein levels after treatment with 100 μ g/mL PEVs (with 200 μ M H₂O₂ stimulation) and 100 μ g/mL PLTs. β actin was used as a loading control. Uncropped gel is in SI Fig. 4C. (D) Quantitative analysis of mitochondrial functional protein expression differences in each group. (E–F) Fluorescence intensity and quantitative analysis of mitochondria using MitoSOX Red staining. Scale bar = 50 μ m. Significance between four groups was calculated using one-way ANOVA with Tukey’s post-hoc test. Data are presented as mean \pm SD (n = 3). (Scale bars are listed above; *: P < 0.05, **: P < 0.01, ***: P < 0.005, and ****: P < 0.001).

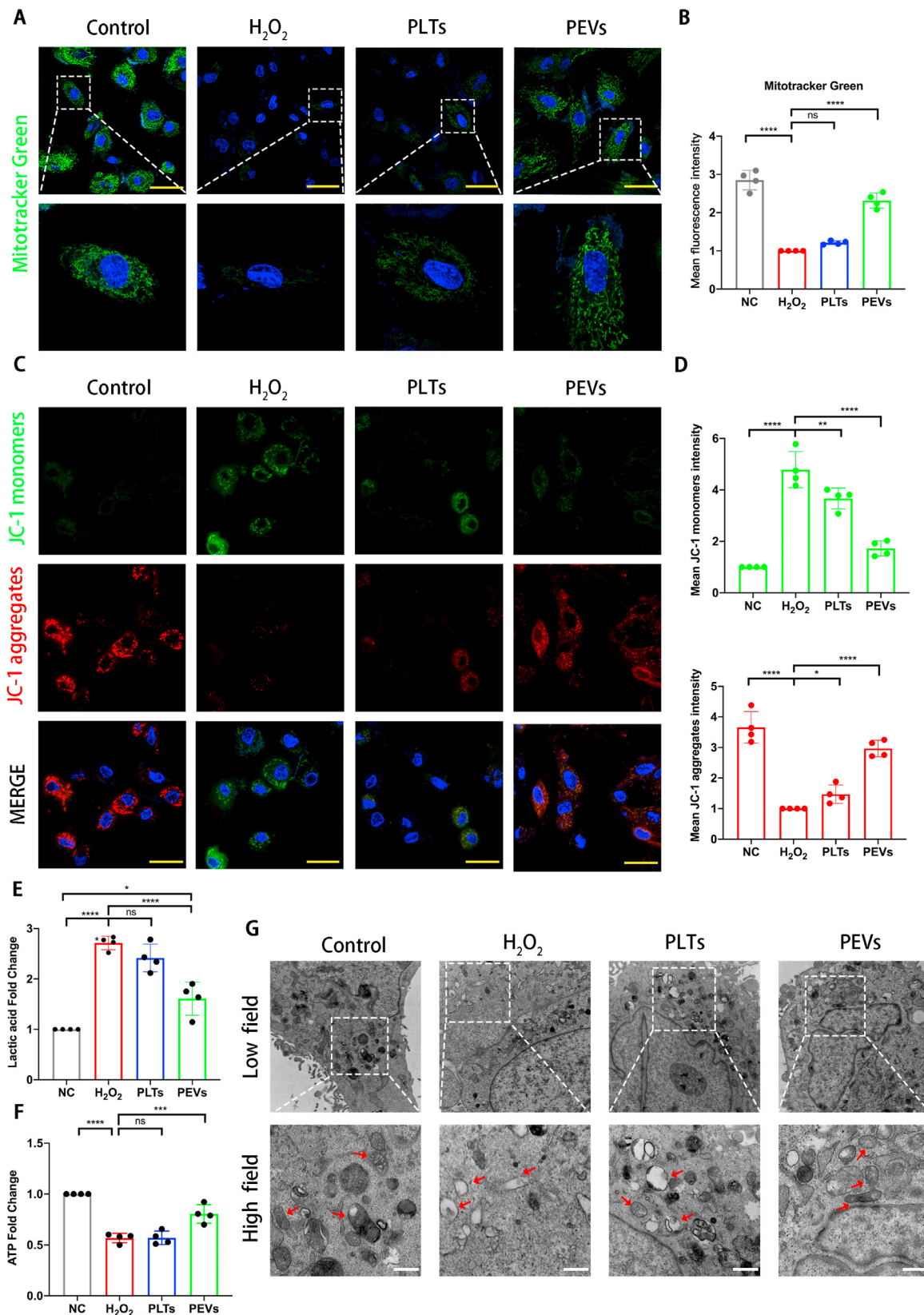


Fig. 8. PEVS restored mitochondrial membrane potential homeostasis and mitochondrial function. Scale bar = 20 μ m. (A) Protective effect of PEVS was evaluated by MitoTracker Green. (B) Quantification of fluorescence intensities according to (A). (C) Detection of mitochondrial membrane potentials in four groups of cells by JC-1 fluorescence probe. Scale bar = 50 μ m. (D) Quantification of fluorescence intensities according to (C). (E) Detection of lactic acid content in supernatant of NP cells culture medium. (F) ATP levels of NP cells was detected. (G) Transmission electron microscopy (TEM) images of mitochondria in NP cells. Scale bar = 0.5 μ m. Significance between four groups was calculated using one-way ANOVA with Tukey's post-hoc test. Data are presented as mean \pm SD (n = 4). (Scale bars are listed above; *: $P < 0.05$, **: $P < 0.01$, ***: $P < 0.005$, and ****: $P < 0.001$).

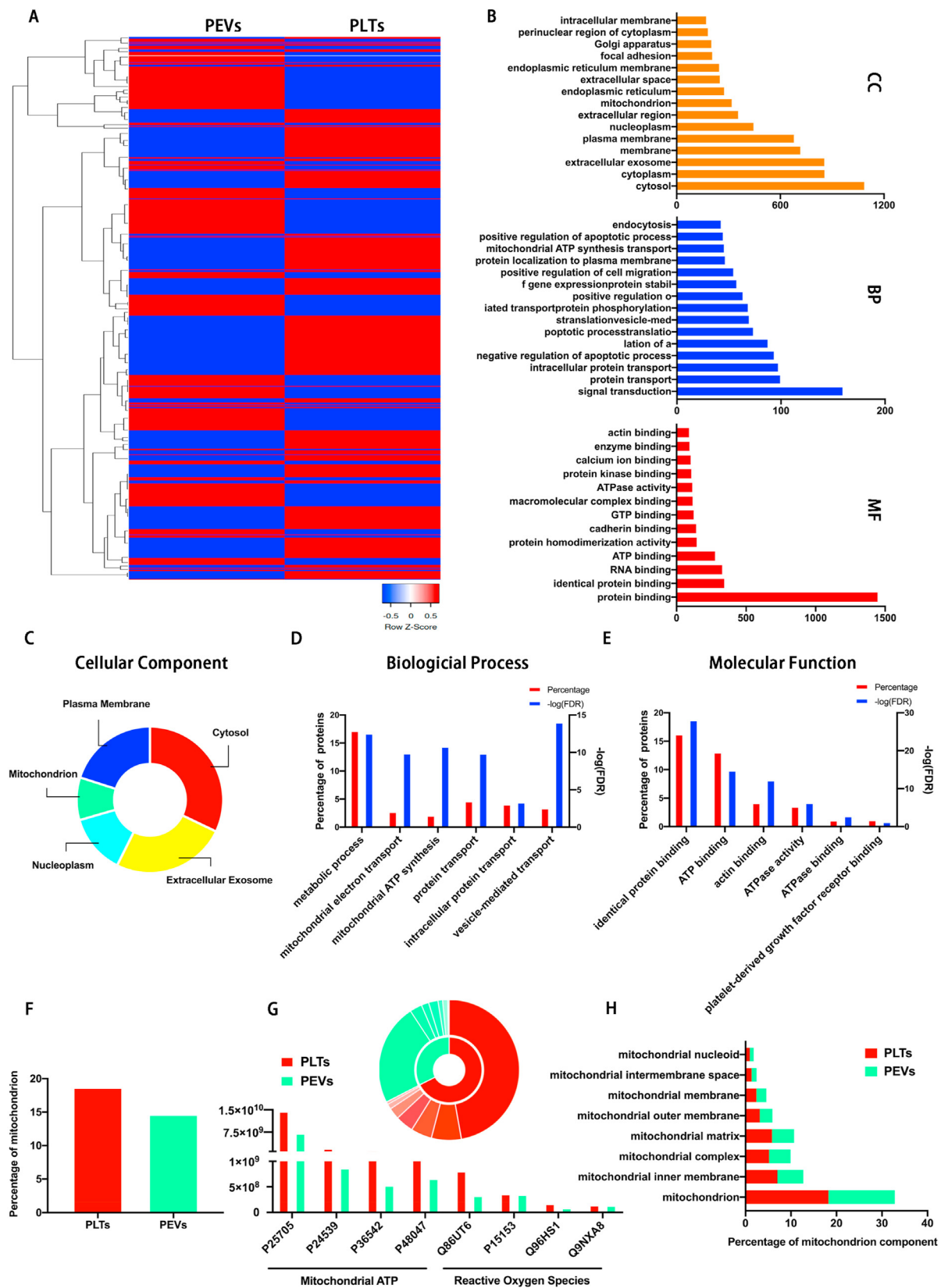
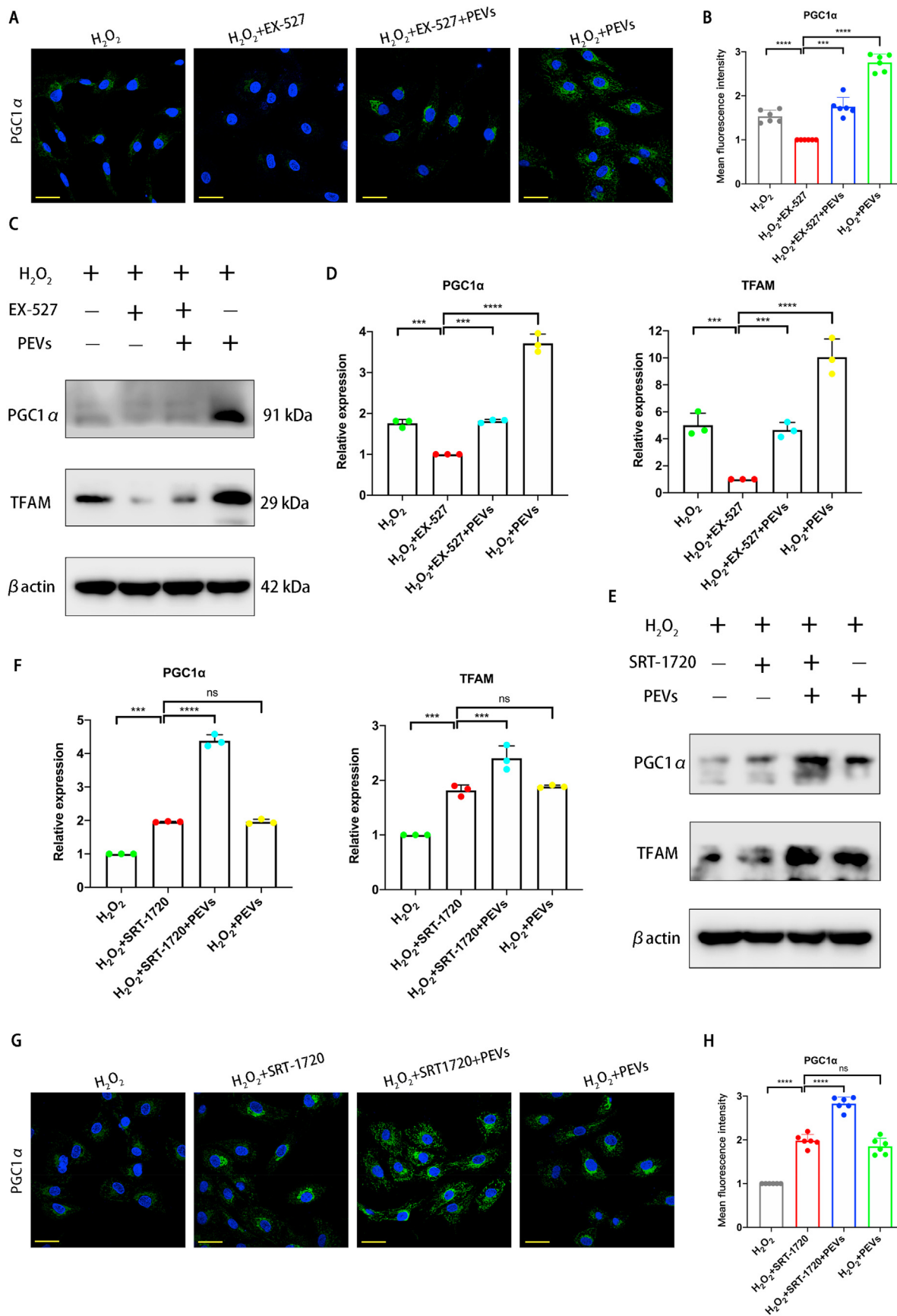


Fig. 9. Proteomic analysis of PEVs and PLTs. (A) Heat map of 1732 parental proteins in PEVs and PLTs. (B) GO classification of parental proteins in biological process, molecular function, and cellular component. (C–E) GO classification of PEVs proteins in cellular component, biological process, and molecular function. (F) Comparison of mitochondrial contents in PLTs and PEVs. (G) The content and categories of proteins in PLTs and PEVs involved in mitochondrial ATP and reactive oxygen species (ROS). (H) Summary of significantly enriched GO terms in mitochondrial content of PLTs and PEVs.



(caption on next page)

Fig. 10. Regulation of mitochondrial function by PEVs via SIRT1 in pathological NP cells. (A) Effects of EX-527 (the selective SIRT1 inhibitor) on the fluorescence expression of mitochondrial functional protein PGC1 α in each group. Scale bar = 50 μ m. (B) Quantification of specific immunofluorescence intensities according to (A). (C) Western blot analysis showing the effects of EX-527 on PGC1 α and TFAM protein levels in pathological NP cells. β actin was used as loading control. Uncropped gel is in SI Fig. 4D. (D) Quantitative analysis of mitochondrial functional protein levels in each group. (E) Western blot analysis showing the effects of SRT-1720 (the selective SIRT1 activator) on PGC1 α and TFAM protein levels in pathological NP cells. β actin was used as loading control. Uncropped gel is in SI Fig. 4E. (F) Quantitative analysis of mitochondrial functional protein levels in each group. (G) Effects of SRT-1720 on the fluorescence expression of mitochondrial functional protein PGC1 α in each group. Scale bar = 50 μ m. (H) Quantification of specific immunofluorescence intensities according to (G). Significance between four groups was calculated using one-way ANOVA with Tukey's post-hoc test. Data are presented as mean \pm SD (n = 3). (Scale bars are listed above; *, $P < 0.05$, **, $P < 0.01$, ***, $P < 0.005$, and ****, $P < 0.001$).

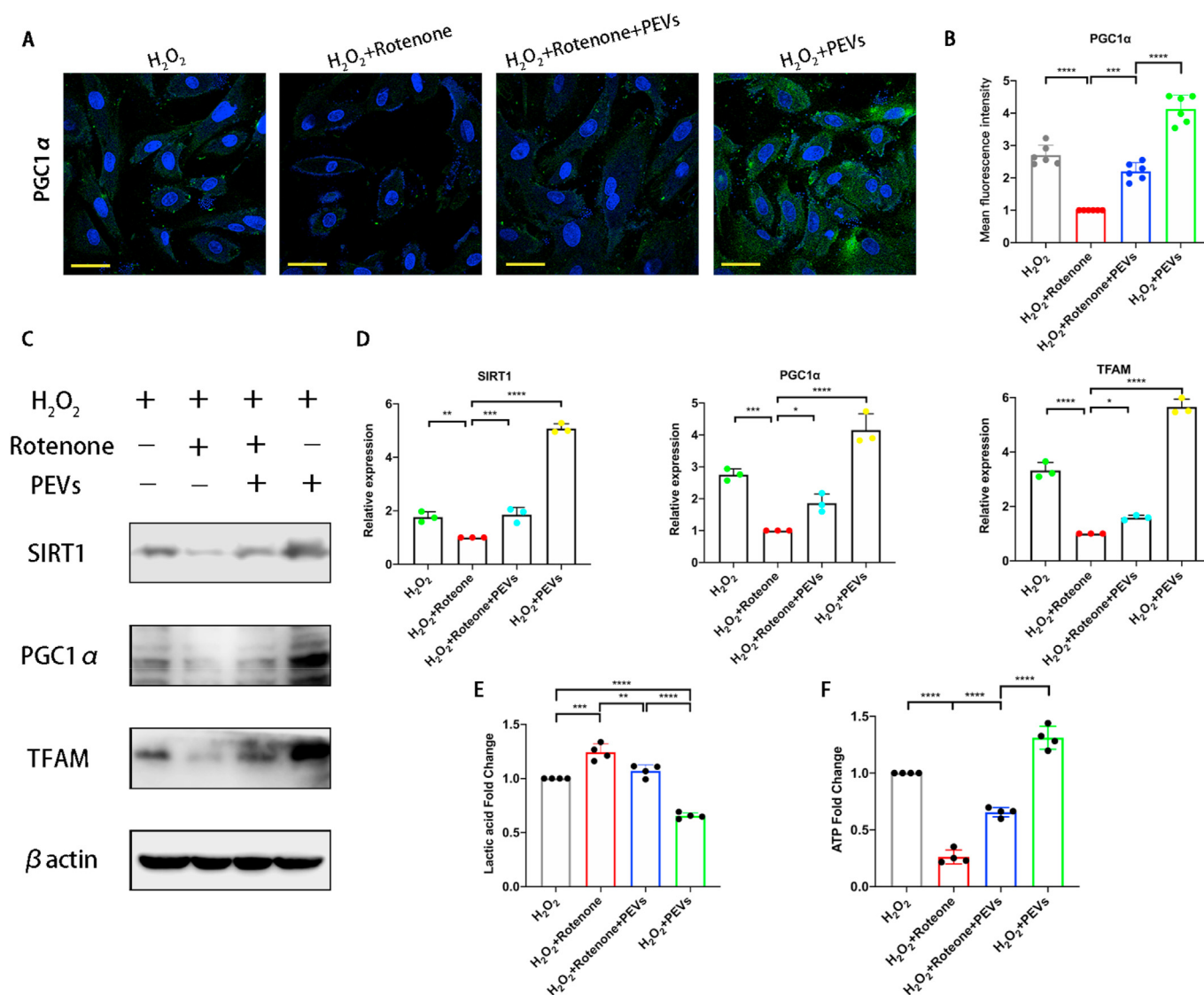


Fig. 11. Effect of rotenone on PEVs treated pathological NP cells. (A) Effects of the inhibitor rotenone on the fluorescence expression of mitochondrial functional protein PGC1 α in each group. Scale bar = 50 μ m. (B) Quantification of specific immunofluorescence intensities according to (A). (C) Western blot analysis showing the effects of rotenone on SIRT1, PGC1 α , and TFAM protein levels in pathological NP cells. β actin was used as loading control. Uncropped gel is in SI Fig. 4F. (D) Quantitative analysis of mitochondrial functional protein levels in each group. (E) Detection of lactic acid concentration in supernatant of pathological NP cells culture medium. (F) ATP levels of pathological NP cells were detected. Significance between four groups was calculated using one-way ANOVA with Tukey's post-hoc test. Data are presented as mean \pm SD (n = 3). (Scale bars are listed above; *, $P < 0.05$, **, $P < 0.01$, ***, $P < 0.005$, and ****, $P < 0.001$).

compared to that in the PLTs group. Overall, these data suggested that PEVs can suppress matrix degradation *in vivo*.

Then we used DHE fluorescent probe to evaluate the effect of PEVs on ROS levels of NP tissue in rat IVD (Fig. 14E and F). The ROS level of NP tissue, which is indicated by the red fluorescence intensity, was low in the NC group and significantly increased after the puncture. The PEVs group showed a significantly downregulated ROS level compared with the PLTs group although the PLTs group exhibited a slight effect in

reducing the ROS level. The result suggested that PEVs can attenuate ROS levels of NP tissue *in vivo*.

Next, we performed frozen histological section experiments to observe ROS levels of mitochondria in rat IVD. We utilized MitoSOX Red staining to detect the effect of PEVs on the ROS levels of mitochondria of rats IVD (Fig. 14G and H). The ROS level of mitochondria is low in the NC group and gradually increased in the vehicle group. Moreover, ROS production indicated by MitoSOX Red staining in the PEVs group was

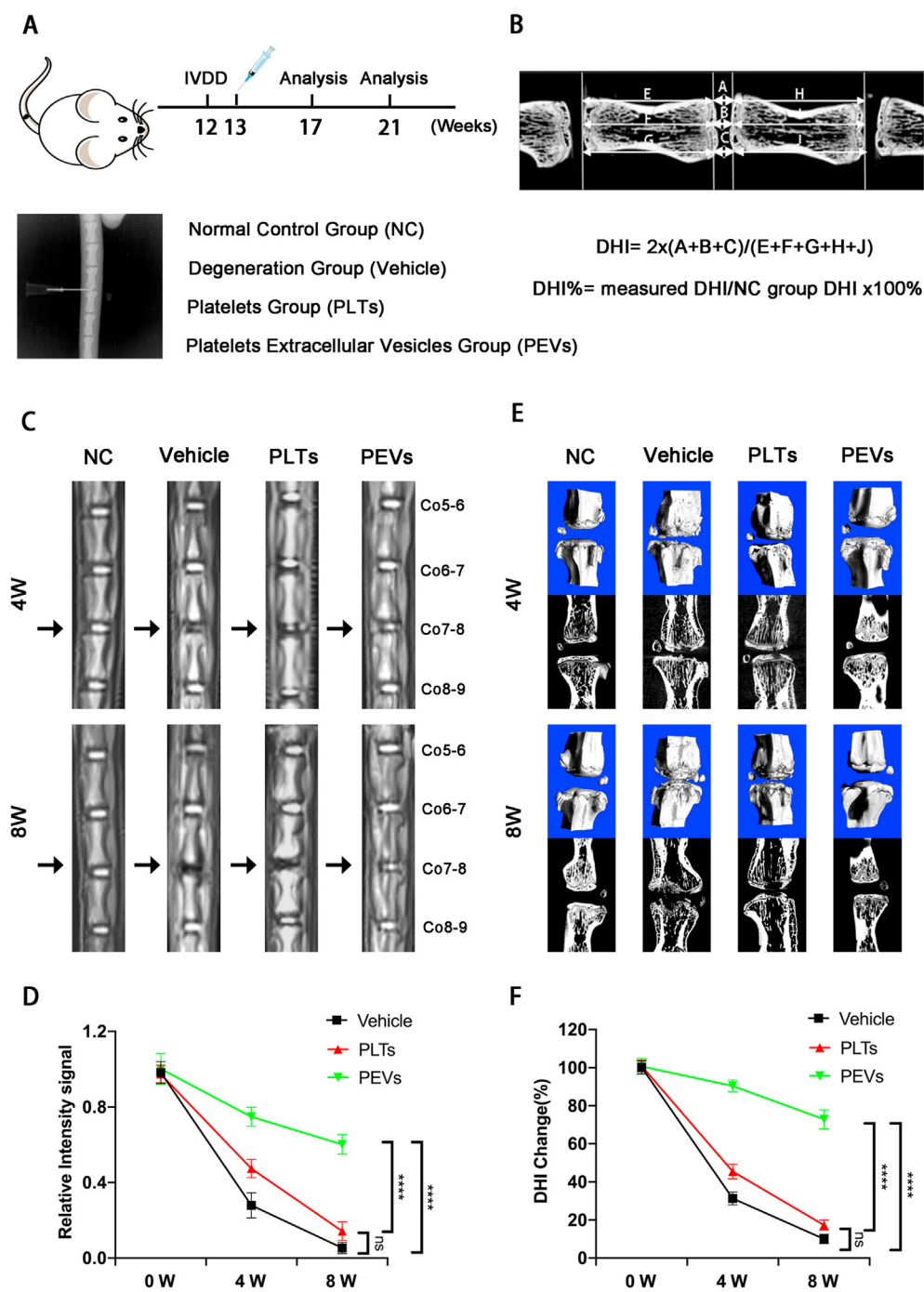


Fig. 12. Radiological data of IVDD rat experiments by the imaging system. (A) Overview of animal experiments and x-ray view of the puncture modeling in the IVDD rat. (B) Measurement and calculation formula of intervertebral disc height index in rat. (C) Representative MRI images of rat caudal vertebrae at 4 and 8 weeks. (The arrow represents the nucleus pulposus (NP)). (D) Quantitative analysis of T2-weighted signal intensity of the NP in each group. (E) Representative Micro-CT images of the caudal vertebrae of rats at 4 and 8 weeks. (F) Change in DHI% in each group. Significance between four groups was calculated using two-way ANOVA with Tukey's post-hoc test. Data are presented as mean ± SD (n = 9). (*: $P < 0.05$, **: $P < 0.01$, ***: $P < 0.005$, and ****: $P < 0.001$).

significantly lower than that in degenerated IVD group (vehicle group) and PLTs group. These results indicate that PEVs can reduce ROS levels of mitochondria in rats IVD.

PGC1 α is the major regulator of mitochondrial biogenesis in the AMPK-SIRT1-PGC1 α -TFAM pathway, and it is the most representative mitochondrial functional protein [93]. Then, we detected PGC1 α abundance in the rat IVD to determine the repairing effect of PEVs on the mitochondria *in vivo*. Compared to the NC group, which showed higher levels of PGC1 α , the vehicle and PLTs groups showed a significant reduction in PGC1 α levels (Fig. 14G, I). However, the PEVs group showed significantly higher PGC1 α fluorescence intensity than the Vehicle and PLTs groups. These results suggest that PEVs promote the restoration of the mitochondrial function to maintain the homeostasis of IVD tissues.

We also evaluated mitochondrial morphology on NP tissue after 8 weeks by TEM and quantified the percentage of mitochondrial vacuoles (Fig. 14J). The results showed that the percentage of mitochondrial vacuoles/mitochondria in PEVs group was markedly lower than in the vehicle and PLTs groups. In other words, the data suggest that PEVs can reduce ROS level and restore mitochondrial function *in vivo*. A schematic of PEVs regulating mitochondrial pathway to promote the repair of damaged mitochondria (Fig. 15).

4. Discussion

In this study, we developed an efficient strategy for IVDD treatment by injecting PEVs. The three major findings are as follows: 1. "Artificial

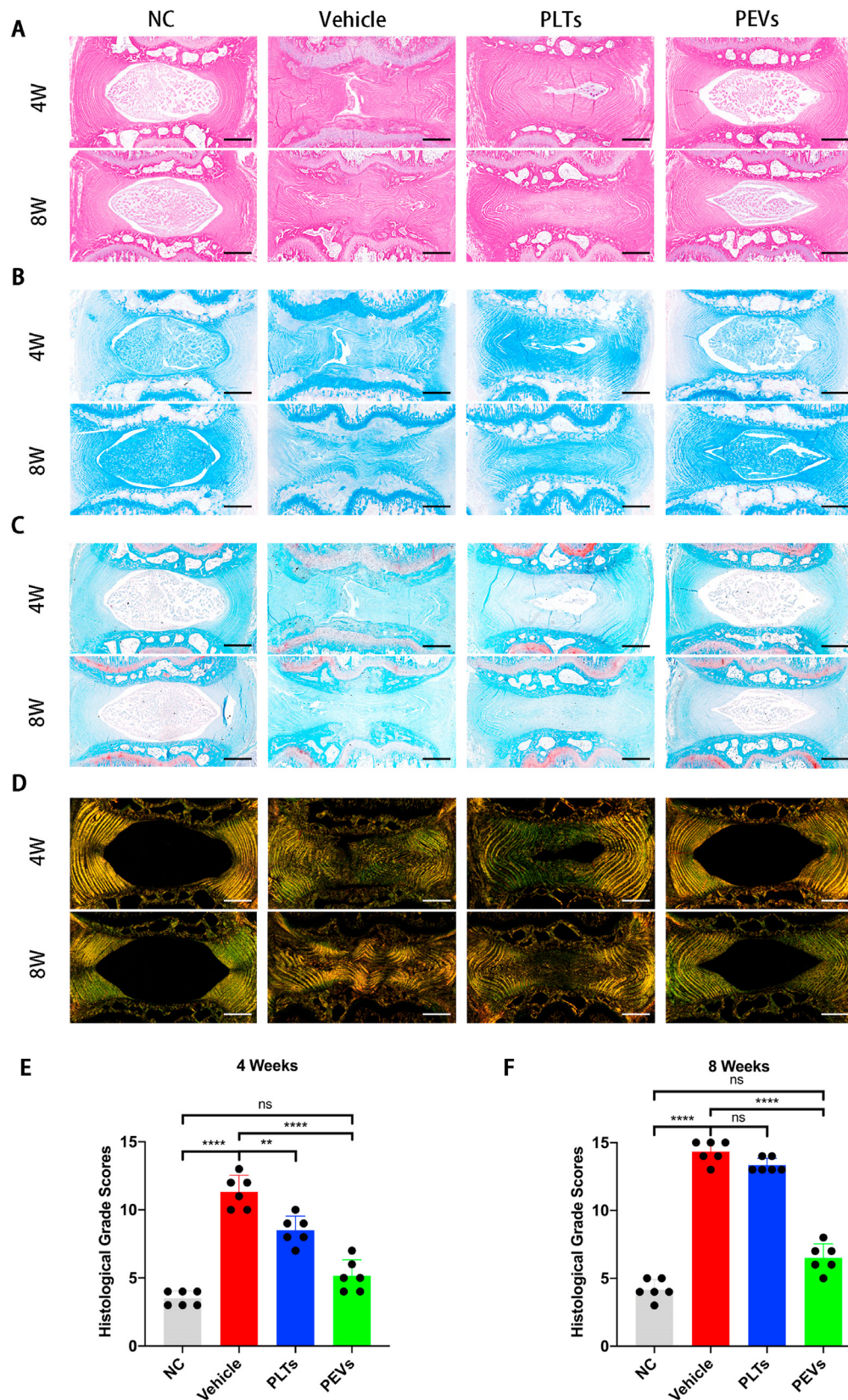
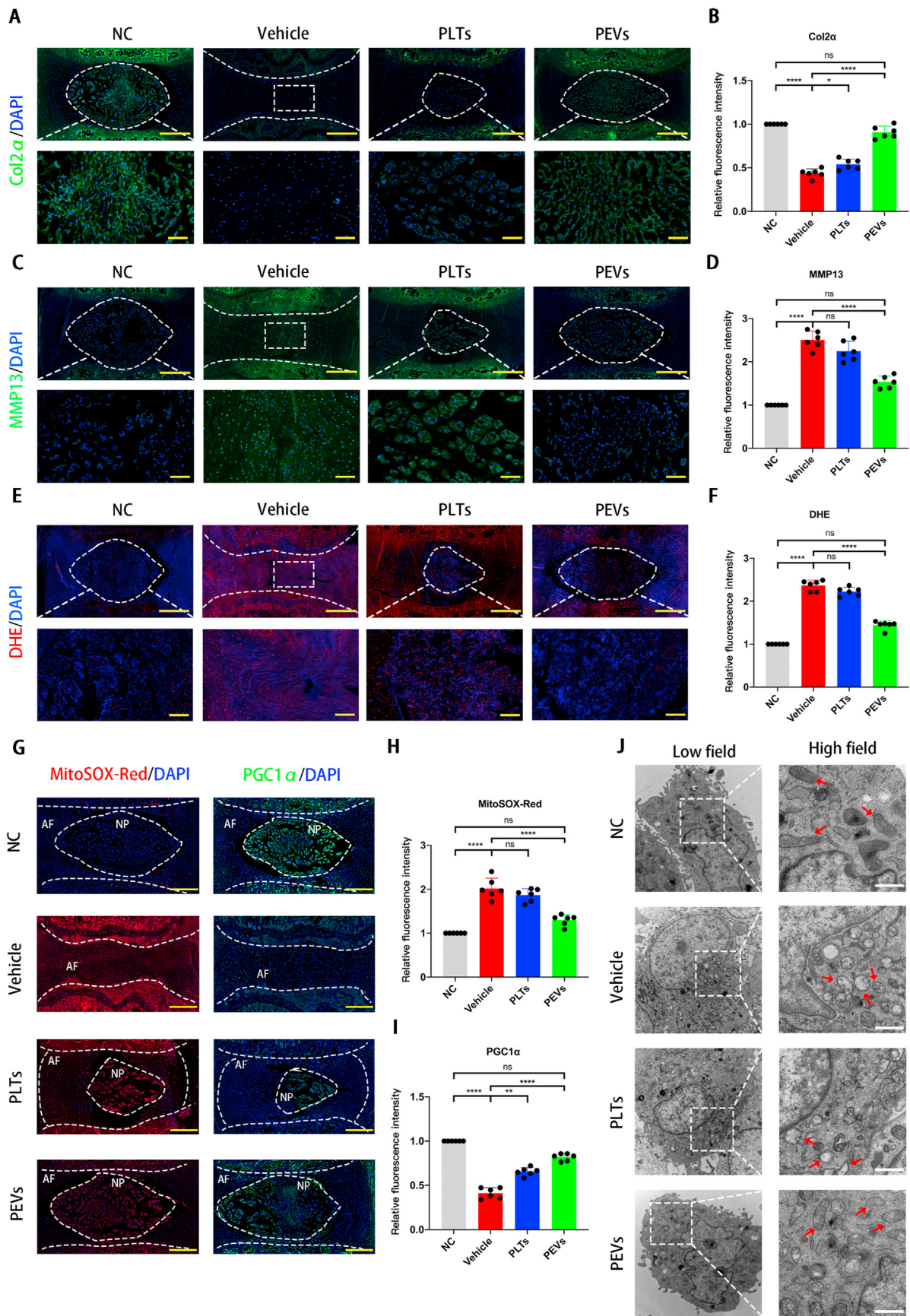


Fig. 13. Histological evaluation of the IVDD rat experiment. (A) The H&E staining images of intervertebral discs of rats at 4 and 8 weeks. (B) Alcian blue staining images. (C) Safranin O-Fast Green staining images. (D) Sirius Red staining images. (E–F) Changes of histological grades evaluation at 4 and 8 weeks in each group. Significance between four groups was calculated using one-way ANOVA with Tukey's post-hoc test. Data are presented as mean \pm SD (n = 6). (Scale bars = 400 μ m; *: $P < 0.05$, **: $P < 0.01$, ***: $P < 0.005$, and ****: $P < 0.001$).



(caption on next page)

Fig. 14. Effects of PEVs on the mitochondrial function of IVD *in vivo*. (A) Immunofluorescence staining images of Col2 α of intervertebral discs (IVD). (B) Quantification of specific immunofluorescence intensities according to Col2 α . (C) Immunofluorescence staining images of MMP13 of IVD. (D) Quantification of specific immunofluorescence intensities according to MMP13. (E) Immunofluorescence staining images of DHE on ROS levels in nucleus pulposus in rat IVD. (F) Quantification of specific immunofluorescence intensities according to DHE. (G) Fluorescent staining images of MitoSox Red and PGC1 α in rats IVD. (H) Quantification of intensities according to MitoSox Red. (I) Quantification of specific immunofluorescence intensities according to PGC1 α . (J) Transmission electron microscopy (TEM) images of mitochondrial morphology in NP cells in rats IVD. Scale bar = 0.5 μ m. Significance between four groups was calculated using two-way ANOVA with Tukey's post-hoc test. Data are presented as mean \pm SD (n = 6). (Scale bars = 400 μ m; *, P < 0.05, **, P < 0.01, ***, P < 0.005, and ****: P < 0.001). Complete slides (A, C, E, G, and H) are in SI Fig. 5.

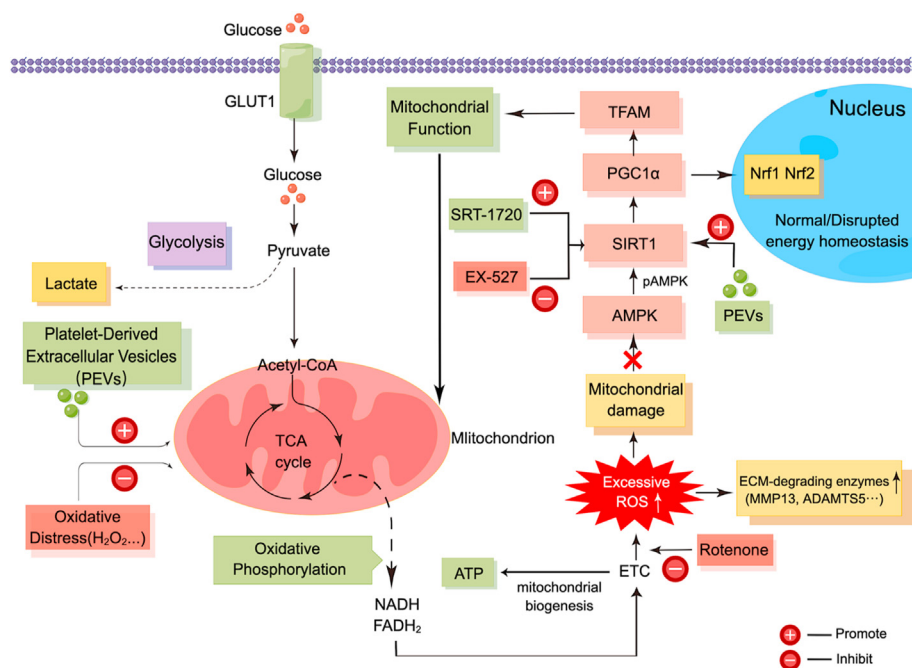


Fig. 15. The schematic of PEVs regulating mitochondrial function to promote the repair of impaired mitochondria. Glycolysis, oxidative phosphorylation, and the AMPK–SIRT1–PGC1 α –TFAM pathway helps to maintain an optimal level of mitochondrial function and intracellular homeostasis in healthy NP cells. In degenerated NP cells, oxidative distress damage and reactive oxygen species (ROS) accumulate, causing damage to the mitochondria, thereby inhibiting AMPK signaling and activity, downregulating SIRT1, decreasing levels of PGC1 α and TFAM, and further impairing the mitochondrial function in NP cells. GLUT1, glucose transporter type 1; TCA, tricarboxylic acid; ETC, electron transport chain; ROS, reactive oxygen species; ATP, adenosine-5'-triphosphate; AMPK, AMP-activated protein kinase; SIRT1, NAD-dependent protein deacetylase sirtuin-1; PGC1 α , peroxisome proliferator-activated receptor γ co-activator 1 α ; TFAM, Mt transcription factor A; Nrf1, nuclear respiratory factor 1; Nrf2, nuclear respiratory factor 2; PEVs, platelet-derived extracellular vesicles; SRT-1720, the selective SIRT1 activator; EX-527, the selective SIRT1 inhibitor.

EVs" prepared by membrane extrusion are good substitutes for cell-derived natural extracellular vesicles. 2. PEVs can alleviate oxidative stress damage and promote the repair of damaged mitochondria in NP cells by activating the SIRT1–PGC1 α –TFAM pathway *in vitro*. 3. Currently, no related research on PEVs in treating rat IVDD exists. We injected PEVs into IVD of rats and validated the retardation effect of PEVs on the degeneration of NP in rats. These findings suggest that the injection of PEVs may be a promising strategy for the treatment of IVDD.

Recent studies have found that PEVs possess molecular markers on their surface such as CD9, CD81, and CD63, which promote intercellular and intracellular signaling and mediate the targeting of PEVs to sites of inflammation, thrombosis, and tumors [94]. Further, studies have reported that PEVs can regulate cell function by delivering proteins, lipids, nucleic acids, and other biologically active molecules to target cells for intercellular communication [45]. Moreover, the function of PEVs in the regulation of tissue repair has been evaluated [95]. The PEVs can cross tissue barriers in the human body, such as the synovium, lymph, and bone marrow because of their 100–200 nm size and phospholipid bilayer structure, and therefore, they are easily absorbed by tissues or cells [37]. Our study found that PEVs can be internalized by NP cells through the actin-mediated endocytosis pathway and localized to the mitochondria.

During bone metabolism, the NP cells utilize glucose and other metabolites as energy sources. These cells generate energy through glycolysis and oxidative phosphorylation of glucose to maintain optimal mitochondrial function [91]. We found that PEVs regulated cellular metabolism by activating the AMPK–SIRT1–PGC1 α –TFAM pathway to maintain mitochondrial homeostasis. The mitochondria are the main producers of ROS in the cells [64]. The accumulation of intracellular ROS can regulate cellular metabolism, ATP production, and synthesis of

nuclear and mitochondrial DNA-encoded genes [96]. However, excessive ROS levels can lead to oxidative stress damage, which further results in mitochondrial dysfunction [97]. Anabolic proteins are upregulated, and catabolic proteins are downregulated when intracellular ROS levels are elevated [98,99]. Depolarized mitochondria are characterized by an imbalance in $\Delta\Psi_m$, and this is an early event in apoptosis [100]. Moreover, aging-related diseases are caused by dysfunctional mitochondria that fail to provide cellular energy [101]. In this study, we verified that H₂O₂ stimulation causes ROS accumulation in NP cells. Moreover, H₂O₂ induced the upregulation of Mmp3, Mmp13, and Adamts5 protein levels and downregulated Col2 α , Aggrecan, and Sox9 protein levels. Further, the levels of mitochondria-related proteins (SIRT1, PGC1 α , TFAM, Nrf1, and Nrf2) were reduced in NP cells after H₂O₂ stimulation. H₂O₂ could impair cellular metabolism by disrupting mitochondrial protein levels, which leads to the degeneration of the ECM and eventually IVDD.

Based on previous studies and references [71,91], AMPK, SIRT1, PGC1 α , and TFAM were defined as mitochondrial-related proteins. These proteins are key regulators of metabolism in the mitochondrion of NP cells. The key protein to regulate mitochondrial function of cells is AMPK, which regulates energy metabolism and intracellular homeostasis through the downstream mediators, SIRT1, PGC1 α , which is the expert regulator of mitochondrial biogenesis and TFAM [102]. The mitochondrial dysfunction in cells is linked to the decreased expression of SIRT1, PGC1 α , TFAM, Nrf1, and Nrf2, respectively. The activation of the AMPK–SIRT1–PGC1 α –TFAM pathway promotes the homeostasis of energy metabolism and mitochondrial function in cells, further limiting the progression of degenerative diseases [71,103,104]. Moreover, a study has demonstrated that SIRT1 can play an essential role in the protection of mitochondrial function both *in vitro* and *in vivo* [105]. The increased

expression of SIRT1 might be a new therapeutic approach for degenerative diseases [106–108].

After a series of *in vitro* and *in vivo* studies, we found that PEVs could modulate the SIRT1–PGC1 α –TFAM pathway, which helps maintain the homeostasis of the IVD. We showed that PEVs could attenuate oxidative stress and inflammation in NP cells. Further, we showed that PEVs decreased the levels of catabolic proteins and elevated those of anabolic proteins. In addition, PEVs can retain some growth factors and mitochondrial proteins from PLTs [30]. We found that their mitochondrial proteins were similar by comparing the proteomic analyses of PEVs and PLTs. Therefore, we tested the effect of PEVs on the expression of mitochondria-related proteins in NP cells, and the results showed that PEVs promoted the abundance of these mitochondrial proteins. In rat IVDD models, we verified that PEVs could retard IVDD, and these results were consistent with those of cellular experiments.

Over the past few years, studies have consistently concluded that PEVs can be inflammation-targeted and play an important role in inter-cellular communication [37,45]. However, the current therapeutic strategies for PEVs continue to face a few challenges in basic research. The cellular origin of PEVs is critical; we must identify the safest cell source for PEVs to avoid immunogenicity issues and ensure that PEVs do not produce toxic components. In addition, we must minimize off-target effects by balancing the natural processing and degradation processes of PEVs when designing therapeutic strategies for specific targets. Appropriate preclinical models must be established, and specific biological processes, cellular components, and molecular functions must be selected to address these issues. The current study demonstrated that PEVs can be phagocytosed and targeted to the mitochondria in NP cells, which helps provide mitochondria-associated proteins to restore their function. During this process, the PEVs alleviate oxidative stress, inhibit cellular inflammation, and restore mitochondrial function to maintain homeostasis in the IVDD. This was similar to previous studies showing that PEVs could enhance wound or tissue healing by improving mitochondrial function and promoting musculoskeletal or nerve regeneration by inducing cell differentiation [44,109,110]. In the emerging field of nanomaterial therapy research, PEVs provide pivotal insights into degenerative diseases associated with the homeostasis of mitochondrial function.

5. Conclusion

We demonstrated that PEVs with high antioxidant activity and inflammatory targeting could retard the progression of IVDD by reducing oxidative stress and inflammatory response. Moreover, PEVs could activate the SIRT1–PGC1 α –TFAM pathway to maintain mitochondrial function. Our results showed that the injection of PEVs can be a promising strategy for treating patients with IVDD.

Credit author statement

Zhanqiu Dai and Chen Xia: Conceptualization, Methodology, Data Curation, and Writing-Original Draft; Tingxiao Zhao: Methodology and Data Curation; Haoli Wang and Hongsen Tian: Formal analysis and Data Curation; Ouyuan Xu: Methodology and Data Curation; Pengfei Chen, Jun Zhang and Xunbin Zhu: Supervision, Project administration, Funding acquisition, and Writing -Review & Editing.

Funding

The study was supported by the National Nature Science Fund of China (Grant No. 82072414 and U21A20351), the National Key R&D Program of China (Grant No. 2020YFC1107104), the Natural Science Fund of Zhejiang Province (Grant No. LY21H060002), the Innovative Talent Support Program Project of Zhejiang Provincial Health Commission (Grant No. 2021433298), the Public Projects of Zhejiang Province (LGF19H060013 and LGD22H060004), the Key research and

development plan in Zhejiang Province (Grant No. 2020C03043), and the Zhejiang Provincial Program for the cultivation of high-level innovative health talents. We thank Wu Lingyun and Yang Ping in the Center of Cryo-Electron Microscopy (CCEM), Zhejiang University for their technical assistance on cryo-TEM.

Declaration of competing interest

The authors declare that they have no known competing financial interests or personal relationships that could have appeared to influence the work reported in this paper. Graphical Abstract and Figure 1 were created using Figdraw (www.figdraw.com). Figures 2A, 4E, 15, 12A, and SI Figure 1 were created with biorender.com.

Data availability

No data was used for the research described in the article.

Appendix A. Supplementary data

Supplementary data to this article can be found online at <https://doi.org/10.1016/j.mtbio.2022.100512>.

References

- [1] N.N. Knezevic, et al., Low back pain, *Lancet* 398 (10294) (2021) 78–92.
- [2] J. Hartvigsen, et al., What low back pain is and why we need to pay attention, *Lancet* 391 (10137) (2018) 2356–2367.
- [3] T. Vos, et al., Years lived with disability (YLDs) for 1160 sequelae of 289 diseases and injuries 1990–2010: a systematic analysis for the Global Burden of Disease Study 2010, *Lancet* 380 (9859) (2012) 2163–2196.
- [4] M. Kanayama, et al., Cross-sectional magnetic resonance imaging study of lumbar disc degeneration in 200 healthy individuals, *J. Neurosurg. Spine* 11 (4) (2009) 501–507.
- [5] K.M. Cheung, et al., Prevalence and pattern of lumbar magnetic resonance imaging changes in a population study of one thousand forty-three individuals, *Spine* 34 (9) (2009) 934–940.
- [6] S. Roberts, et al., Histology and pathology of the human intervertebral disc, *J Bone Joint Surg Am* 88 (Suppl 2) (2006) 10–14.
- [7] B.L. Chen, et al., Surgical versus non-operative treatment for lumbar disc herniation: a systematic review and meta-analysis, *Clin. Rehabil.* 32 (2) (2018) 146–160.
- [8] D. Yavin, et al., Lumbar fusion for degenerative disease: a systematic review and meta-analysis, *Neurosurgery* 80 (5) (2017) 701–715.
- [9] A. Pan, et al., Adjacent segment degeneration after lumbar spinal fusion compared with motion-preservation procedures: a meta-analysis, *Eur. Spine J.* 25 (5) (2016) 1522–1532.
- [10] K. Hashimoto, et al., Adjacent segment degeneration after fusion spinal surgery—a systematic review, *Int. Orthop.* 43 (4) (2019) 987–993.
- [11] A. Rogerson, J. Aidlen, L.G. Jennis, Persistent radiculopathy after surgical treatment for lumbar disc herniation: causes and treatment options, *Int. Orthop.* 43 (4) (2019) 969–973.
- [12] R.D. Bowles, L.A. Setton, Biomaterials for intervertebral disc regeneration and repair, *Biomaterials* 129 (2017) 54–67.
- [13] B. Lukomska, et al., Challenges and controversies in human mesenchymal stem cell therapy, *Stem Cell. Int.* 2019 (2019), 9628536.
- [14] C. Xia, et al., Mesenchymal stem cell-derived exosomes ameliorate intervertebral disc degeneration via anti-oxidant and anti-inflammatory effects, *Free Radic. Biol. Med.* 143 (2019) 1–15.
- [15] Z. Liao, et al., Exosomes from mesenchymal stem cells modulate endoplasmic reticulum stress to protect against nucleus pulposus cell death and ameliorate intervertebral disc degeneration *in vivo*, *Theranostics* 9 (14) (2019) 4084–4100.
- [16] H. Xing, et al., Injectable exosome-functionalized extracellular matrix hydrogel for metabolism balance and pyroptosis regulation in intervertebral disc degeneration, *J. Nanobiotechnol.* 19 (1) (2021) 264.
- [17] C. He, et al., Exosome theranostics: biology and translational medicine, *Theranostics* 8 (1) (2018) 237–255.
- [18] P. Everts, et al., Platelet-rich plasma: new performance understandings and therapeutic considerations in 2020, *Int. J. Mol. Sci.* 21 (20) (2020).
- [19] K. Akeda, et al., Platelet-rich plasma in the management of chronic low back pain: a critical review, *J. Pain Res.* 12 (2019) 753–767.
- [20] Y. Chang, et al., Effect of platelet-rich plasma on intervertebral disc degeneration *in vivo* and *in vitro*: a critical review, *Oxid. Med. Cell. Longev.* 2020 (2020), 8893819.
- [21] P. Oneto, J. Etulain, PRP in wound healing applications, *Platelets* 32 (2) (2021) 189–199.
- [22] P.A. Everts, et al., Platelet rich plasma in orthopedic surgical medicine, *Platelets* 32 (2) (2021) 163–174.

- [23] S. Gupta, A. Paliczak, D. Delgado, Evidence-based indications of platelet-rich plasma therapy, *Expert Rev. Hematol.* 14 (1) (2021) 97–108.
- [24] K. Beitzel, et al., US definitions, current use, and FDA stance on use of platelet-rich plasma in sports medicine, *J. Knee Surg.* 28 (1) (2015) 29–34.
- [25] F. Zallio, et al., A single-center pilot prospective study of topical application of platelet-derived eye drops for patients with ocular chronic graft-versus-host disease, *Biol. Blood Marrow Transplant.* 22 (9) (2016) 1664–1670.
- [26] P.A. Everts, et al., Differences in platelet growth factor release and leucocyte kinetics during autologous platelet gel formation, *Transfus. Med.* 16 (5) (2006) 363–368.
- [27] K.R. Machlus, J.E. Italiano Jr., The incredible journey: from megakaryocyte development to platelet formation, *J. Cell Biol.* 201 (6) (2013) 785–796.
- [28] M. Holinstat, Normal platelet function, *Cancer Metastasis Rev.* 36 (2) (2017) 195–198.
- [29] T. Gremmel, A.L. Frelinger 3rd, A.D. Michelson, Platelet physiology, *Semin. Thromb. Hemost.* 42 (3) (2016) 191–204.
- [30] J. Levoux, et al., Platelets facilitate the wound-healing capability of mesenchymal stem cells by mitochondrial transfer and metabolic reprogramming, *Cell Metabol.* 33 (2) (2021) 283–299 e9.
- [31] E. Chen, et al., Platelet-derived respiratory-competent mitochondria transfer to mesenchymal stem cells to promote wound healing via metabolic reprogramming, *Platelets* 33 (2) (2022) 171–173.
- [32] Y.Z. Xiang, et al., Platelet activation, and antiplatelet targets and agents: current and novel strategies, *Drugs* 68 (12) (2008) 1647–1664.
- [33] P.E.J. van der Meijden, J.W.M. Heemskerk, Platelet biology and functions: new concepts and clinical perspectives, *Nat. Rev. Cardiol.* 16 (3) (2019) 166–179.
- [34] M. Koupenova, et al., Circulating platelets as mediators of immunity, inflammation, and thrombosis, *Circ. Res.* 122 (2) (2018) 337–351.
- [35] H.S. Huang, H.H. Chang, Platelets in inflammation and immune modulations: functions beyond hemostasis, *Arch. Immunol. Ther. Exp.* 60 (6) (2012) 443–451.
- [36] A.T. Nurden, The biology of the platelet with special reference to inflammation, wound healing and immunity, *Front Biosci (Landmark Ed)* 23 (4) (2018) 726–751.
- [37] F. Puhm, E. Boilard, K.R. Machlus, Platelet extracellular vesicles: beyond the blood, *Arterioscler. Thromb. Vasc. Biol.* 41 (1) (2021) 87–96.
- [38] B. Estevez, X. Du, New concepts and mechanisms of platelet activation signaling, *Physiology* 32 (2) (2017) 162–177.
- [39] H. Jung, Y.Y. Kang, H. Mok, Platelet-derived nanovesicles for hemostasis without release of pro-inflammatory cytokines, *Biomater. Sci.* 7 (3) (2019) 856–859.
- [40] W. Liao, et al., Exosomes: the next generation of endogenous nanomaterials for advanced drug delivery and therapy, *Acta Biomater.* 86 (2019) 1–14.
- [41] I. Melki, et al., Platelet microvesicles in health and disease, *Platelets* 28 (3) (2017) 214–221.
- [42] E. Boilard, Extracellular vesicles and their content in bioactive lipid mediators: more than a sack of microRNA, *J. Lipid Res.* 59 (11) (2018) 2037–2046.
- [43] T. Burnouf, et al., Platelet microparticles: detection and assessment of their paradoxical functional roles in disease and regenerative medicine, *Blood Rev.* 28 (4) (2014) 155–166.
- [44] S.C. Tao, S.C. Guo, C.Q. Zhang, Platelet-derived extracellular vesicles: an emerging therapeutic approach, *Int. J. Biol. Sci.* 13 (7) (2017) 828–834.
- [45] J. Johnson, et al., Prospective therapeutic applications of platelet extracellular vesicles, *Trends Biotechnol.* 39 (6) (2021) 598–612.
- [46] M.R. Dyer, et al., Platelet-derived extracellular vesicles released after trauma promote hemostasis and contribute to DVT in mice, *J. Thromb. Haemostasis* 17 (10) (2019) 1733–1745.
- [47] G. Marcoux, et al., Platelet-derived extracellular vesicles convey mitochondrial DAMPs in platelet concentrates and their levels are associated with adverse reactions, *Transfusion* 59 (7) (2019) 2403–2414.
- [48] E. Boilard, A.C. Duchez, A. Brisson, The diversity of platelet microparticles, *Curr. Opin. Hematol.* 22 (5) (2015) 437–444.
- [49] J. Xie, et al., Nanomaterial-based blood-brain-barrier (BBB) crossing strategies, *Biomaterials* 224 (2019), 119491.
- [50] A.T. Franco, A. Corken, J. Ware, Platelets at the interface of thrombosis, inflammation, and cancer, *Blood* 126 (5) (2015) 582–588.
- [51] E. Lopez, et al., Platelet-derived extracellular vesicles promote hemostasis and prevent the development of hemorrhagic shock, *Sci. Rep.* 9 (1) (2019), 17676.
- [52] M. Chimen, et al., Appropriation of GPIIb/IIIa from platelet-derived extracellular vesicles supports monocyte recruitment in systemic inflammation, *Haematologica* 105 (5) (2020) 1248–1261.
- [53] L. Daneshmandi, et al., Emergence of the stem cell secretome in regenerative engineering, *Trends Biotechnol.* 38 (12) (2020) 1373–1384.
- [54] B. Zhang, et al., Mesenchymal stem cell-derived extracellular vesicles in tissue regeneration, *Cell Transplant.* 29 (2020), 963689720908500.
- [55] C. Feng, et al., ROS: Crucial Intermediators in the Pathogenesis of Intervertebral Disc Degeneration, vol. 2017, *Oxid Med Cell Longev.* 2017, 5601593.
- [56] G.S. Shadel, T.L. Horvath, Mitochondrial ROS signaling in organismal homeostasis, *Cell* 163 (3) (2015) 560–569.
- [57] R.M. Whitaker, et al., Mitochondrial biogenesis as a pharmacological target: a new approach to acute and chronic diseases, *Annu. Rev. Pharmacol. Toxicol.* 56 (2016) 229–249.
- [58] J.R. Friedman, J. Nunnari, Mitochondrial form and function, *Nature* 505 (7483) (2014) 335–343.
- [59] D.C. Wallace, W. Fan, V. Procaccio, Mitochondrial energetics and therapeutics, *Annu. Rev. Pathol.* 5 (2010) 297–348.
- [60] T. Finkel, The metabolic regulation of aging, *Nat. Med.* 21 (12) (2015) 1416–1423.
- [61] M. Picard, Mitochondrial synapses: intracellular communication and signal integration, *Trends Neurosci.* 38 (8) (2015) 468–474.
- [62] R.E. Koch, C.C. Josefsen, G.E. Hill, Mitochondrial function, ornamentation, and immune competence, *Biol. Rev. Camb. Phil. Soc.* 92 (3) (2017) 1459–1474.
- [63] T.T. Hickman, S. Rathana-Kumar, S.H. Peck, Development, pathogenesis, and regeneration of the intervertebral disc: current and future insights spanning traditional to omics methods, *Front. Cell Dev. Biol.* 10 (2022), 841831.
- [64] J. Dan Dunn, et al., Reactive oxygen species and mitochondria: a nexus of cellular homeostasis, *Redox Biol.* 6 (2015) 472–485.
- [65] A.L. Graca, et al., Therapeutic effects of platelet-derived extracellular vesicles in a bioengineered tendon disease model, *Int. J. Mol. Sci.* 23 (6) (2022).
- [66] L. Liu, Q.J. Deng, Role of platelet-derived extracellular vesicles in traumatic brain injury-induced coagulopathy and inflammation, *Neural Regen Res* 17 (10) (2022) 2102–2107.
- [67] F. Rannou, et al., Intervertebral disc degeneration: the role of the mitochondrial pathway in annulus fibrosus cell apoptosis induced by overload, *Am. J. Pathol.* 164 (3) (2004) 915–924.
- [68] G.R. Steinberg, B.E. Kemp, AMPK in health and disease, *Physiol. Rev.* 89 (3) (2009) 1025–1078.
- [69] B.L. Tang, Sirt1 and the mitochondria, *Mol. Cell.* 39 (2) (2016) 87–95.
- [70] X. Yang, et al., The diabetes medication canagliflozin promotes mitochondrial remodelling of adipocyte via the AMPK-Sirt1-Pgc-Alpha signalling pathway, *Adipocyte* 9 (1) (2020) 484–494.
- [71] Y. Wang, et al., Mitochondrial biogenesis is impaired in osteoarthritis chondrocytes but reversible via peroxisome proliferator-activated receptor gamma coactivator 1alpha, *Arthritis Rheumatol.* 67 (8) (2015) 2141–2153.
- [72] H. Liang, W.F. Ward, PGC-1alpha: a key regulator of energy metabolism, *Adv. Physiol. Educ.* 30 (4) (2006) 145–151.
- [73] G.H. Kunkel, P. Chaturvedi, S.C. Tyagi, Mitochondrial pathways to cardiac recovery: TFAM, *Heart Fail. Rev.* 21 (5) (2016) 499–517.
- [74] W. Yin, et al., Advantages of pure platelet-rich plasma compared with leukocyte- and platelet-rich plasma in promoting repair of bone defects, *J. Transl. Med.* 14 (2016) 73.
- [75] Y. Zhang, et al., Exosomes derived from platelet-rich plasma administration in site mediate cartilage protection in subtalar osteoarthritis, *J. Nanobiotechnol.* 20 (1) (2022) 56.
- [76] S. Zaib, et al., Role of mitochondrial membrane potential and lactate dehydrogenase A in apoptosis, *Anti Cancer Agents Med. Chem.* 22 (11) (2022) 2048–2062.
- [77] H.A. Kalpage, et al., Tissue-specific regulation of cytochrome c by post-translational modifications: respiration, the mitochondrial membrane potential, ROS, and apoptosis, *FASEB J* 33 (2) (2019) 1540–1553.
- [78] K. Elefantova, et al., Detection of the mitochondrial membrane potential by the cationic dye JC-1 in L1210 cells with massive overexpression of the plasma membrane ABCB1 drug transporter, *Int. J. Mol. Sci.* 19 (7) (2018).
- [79] A. Perelman, et al., JC-1: alternative excitation wavelengths facilitate mitochondrial membrane potential cytometry, *Cell Death Dis.* 3 (2012) e430.
- [80] Y. Wan, et al., Aptamer-conjugated extracellular nanovesicles for targeted drug delivery, *Cancer Res.* 78 (3) (2018) 798–808.
- [81] H.S. Kim, et al., Cell-membrane-derived nanoparticles with notch-1 suppressor delivery promote hypoxic cell-cell packing and inhibit angiogenesis acting as a two-edged sword, *Adv. Mater.* 33 (40) (2021) e2101558.
- [82] E. Geurickx, et al., The generation and use of recombinant extracellular vesicles as biological reference material, *Nat. Commun.* 10 (1) (2019) 3288.
- [83] X. Luan, et al., Engineering exosomes as refined biological nanoplatforms for drug delivery, *Acta Pharmacol. Sin.* 38 (6) (2017) 754–763.
- [84] Y.Y. Jhan, et al., Engineered extracellular vesicles with synthetic lipids via membrane fusion to establish efficient gene delivery, *Int. J. Pharm.* 573 (2020), 118802.
- [85] A. Grangier, et al., Technological advances towards extracellular vesicles mass production, *Adv. Drug Deliv. Rev.* 176 (2021), 113843.
- [86] I.D. Pokrovskaya, et al., 3D ultrastructural analysis of alpha-granule, dense granule, mitochondria, and canalicular system arrangement in resting human platelets, *Res Pract Thromb Haemost* 4 (1) (2020) 72–85.
- [87] S. Miwa, et al., Mitochondrial dysfunction in cell senescence and aging, *J. Clin. Invest.* 132 (13) (2022).
- [88] L. Habiballa, H. Salmonowicz, J.F. Passos, Mitochondria and cellular senescence: implications for musculoskeletal ageing, *Free Radic. Biol. Med.* 132 (2019) 3–10.
- [89] M. Zhang, et al., Conscriptio of immune cells by light-activatable silencing NK-derived exosome (LASNEO) for synergetic tumor eradication, *Adv. Sci.* 9 (22) (2022) e2201135.
- [90] H. Zhong, et al., SERPINA1 is a hub gene associated with intervertebral disc degeneration grade and affects the nucleus pulposus cell phenotype through the ADIRF-AS1/miR-214-3p axis, *Transl. Res.* 245 (2022) 99–116.
- [91] A. Mobasheri, et al., The role of metabolism in the pathogenesis of osteoarthritis, *Nat. Rev. Rheumatol.* 13 (5) (2017) 302–311.
- [92] X. Liu, et al., Fusogenic reactive oxygen species triggered charge-reversal vector for effective gene delivery, *Adv. Mater.* 28 (9) (2016) 1743–1752.
- [93] C. Canto, J. Auwerx, PGC-1alpha, SIRT1 and AMPK, an energy sensing network that controls energy expenditure, *Curr. Opin. Lipidol.* 20 (2) (2009) 98–105.
- [94] A. Gasecka, et al., Platelet extracellular vesicles as biomarkers for arterial thrombosis, *Platelets* 28 (3) (2017) 228–234.
- [95] J. Wu, et al., Platelet-rich plasma-derived extracellular vesicles: a superior alternative in regenerative medicine? *Cell Prolif* 54 (12) (2021), e13123.
- [96] H. Li, J. Slone, T. Huang, The role of mitochondrial-related nuclear genes in age-related common disease, *Mitochondrion* 53 (2020) 38–47.

- [97] L. Kang, et al., Restoration of autophagic flux rescues oxidative damage and mitochondrial dysfunction to protect against intervertebral disc degeneration, *Oxid. Med. Cell. Longev.* 2019 (2019), 7810320.
- [98] N.M. Khan, et al., Wogonin, a plant derived small molecule, exerts potent anti-inflammatory and chondroprotective effects through the activation of ROS/ERK/Nrf2 signaling pathways in human Osteoarthritis chondrocytes, *Free Radic. Biol. Med.* 106 (2017) 288–301.
- [99] F. Liebel, et al., Irradiation of skin with visible light induces reactive oxygen species and matrix-degrading enzymes, *J. Invest. Dermatol.* 132 (7) (2012) 1901–1907.
- [100] U. Fearon, et al., Hypoxia, mitochondrial dysfunction and synovial invasiveness in rheumatoid arthritis, *Nat. Rev. Rheumatol.* 12 (7) (2016) 385–397.
- [101] M. Karbowski, A. Neutzner, Neurodegeneration as a consequence of failed mitochondrial maintenance, *Acta Neuropathol.* 123 (2) (2012) 157–171.
- [102] R. Liu-Bryan, R. Terkeltaub, Emerging regulators of the inflammatory process in osteoarthritis, *Nat. Rev. Rheumatol.* 11 (1) (2015) 35–44.
- [103] C. Zhang, et al., Allicin regulates energy homeostasis through Brown adipose tissue, *iScience* 23 (5) (2020), 101113.
- [104] X. Zhao, et al., Peroxisome proliferator-activated receptor gamma coactivator 1alpha and FoxO3A mediate chondroprotection by AMP-activated protein kinase, *Arthritis Rheumatol.* 66 (11) (2014) 3073–3082.
- [105] N.L. Price, et al., SIRT1 is required for AMPK activation and the beneficial effects of resveratrol on mitochondrial function, *Cell Metabol.* 15 (5) (2012) 675–690.
- [106] T. Matsushita, et al., The overexpression of SIRT1 inhibited osteoarthritic gene expression changes induced by interleukin-1beta in human chondrocytes, *J. Orthop. Res.* 31 (4) (2013) 531–537.
- [107] M.H. Moon, et al., SIRT1, a class III histone deacetylase, regulates TNF-alpha-induced inflammation in human chondrocytes, *Osteoarthritis Cartilage* 21 (3) (2013) 470–480.
- [108] Z. Zheng, et al., Ginsenoside Rb1 reduces H2O2-induced HUVEC dysfunction by stimulating the sirtuin1/AMP-activated protein kinase pathway, *Mol. Med. Rep.* 22 (1) (2020) 247–256.
- [109] M. Antich-Rossello, et al., Platelet-derived extracellular vesicles for regenerative medicine, *Int. J. Mol. Sci.* 22 (16) (2021).
- [110] F.G. Gomes, et al., Synergy of human platelet-derived extracellular vesicles with secretome proteins promotes regenerative functions, *Biomedicines* 10 (2) (2022).